ADDITIVE MANUFACTURABLE METASURFACES FOR RF APPLICATION

by

Kristy Alexandra Hecht

A thesis submitted to the faculty of
The University of North Carolina at Charlotte
in partial fulfillment of the requirements
for the degree of Master of Science in
Electrical Engineering

Charlotte

2020

Approved by:

_____
Dr. Mario Junior Mencagli

_____
Dr. Kathryn Smith Weldon

_____
Dr. Edward B. Stokes

ABSTRACT

KRISTY ALEXANDRA HECHT. Additive Manufacturable Metasurfaces for RF Application. (Under the direction of DR. MARIO JUNIOR MENCAGLI)

Materials found in nature exhibit behaviors with certain properties such as mass density, permeability, and permittivity. Unfortunately, there are limitations and restrictions to the behaviors of these materials that can be overcome with the use of metamaterials. To improve the capabilities of metamaterials, three-dimensional metamaterials were created into planar metamaterials called metasurfaces. The transition making them from three-dimensional to two-dimensional resulted in the properties being controlled changing. Whereas three-dimensional electromagnetic metamaterials typically utilize the properties of negative permittivity and negativity permeability, metasurfaces use surface impedance to change properties such as polarization, beam shaping, and angle of reflection.

This thesis examines additive manufacturable metasurfaces through a sinusoidally modulated antenna and polarization splitting metasurface. In order to design the metasurfaces, the ideas of periodicity are explored along with impedance boundary conditions. Using an isotropic impedance boundary condition and periodic unit cells of cylinders of varying heights, the design of a sinusoidally modulated is discussed. The antenna is designed with two different materials to examine the versatility. The metallic antenna is designed for broadside and non-broadside propagation and also simulated with the non-ideal conductive material. The simulation results showed the antenna with a propagation corresponding to its designed parameters. In addition, the non-ideal materials performed almost identically to the PEC antenna.

The metasurface was also designed using periodic boundaries, but utilized a tensor as impedance making the metasurface anisotropic. The metasurface performs as a polarization splitter such that depending on the excitation mode, the angle the beam

is steered is different. This is designed using five different unit cells of varying phases, each with three-layers to introduce an extra degree of freedom for impedance. Results for each unit cell are provided including the magnitude and phase of each unit cell.

Using a commercial 3D printer, the two metasurfaces can be produced easily. The ability of the additive manufacturing electromagnetic devices allows easy access to components with different functions at low cost. Although demonstrated with a center frequency of 15 GHz, the antenna can easily be adapted for a design with any center frequency and pointing angle at the limitations of the preciseness of the additive manufacturing printer. The ability of the adaptable designs allows antennas to be designed for the specific need of the person, such as testing in an anechoic chamber, at a low cost and quick production time. Another advantage of this antenna is the fact that it is excitable with a simple coaxial cable structure in the center of the antenna which cannot be done currently with transmit arrays and other current technologies.

DEDICATION

To Fourier, the best bearded dragon with a life ended way too soon.

ACKNOWLEDGEMENTS

This thesis would not have been possible without the abundance of help I have received along the way.

I would like to express my absolute gratitude to Dr. Mario Junior Mencagli for being an absolutely amazing advisor for both personal and academia. I have been able to flourish under your guidance and I will be forever grateful for how much you have pushed me and helped me learn and better myself.

I would also like to thank my committee members, Dr. Kathryn Smith Weldon and Dr. Edward B. Stokes, for your constructive criticism and the time dedicated to help me succeed.

I am grateful for my lab mates, Matthew Trusnovic and Kristina Moralic, who have assisted me in my research and have helped me talk through my ideas. You have been been amazing emotional support as well!

I want to thank my friends for standing by me and cheering me on from the sidelines. All the support means so much.

I want to extend my utmost gratitude to the two closest people to me in my life. My best friend, Jennifer Gay, has been by my side for over ten years as my biggest supporter in life. She has helped me edit this thesis, but she has also been nonstop support for every adventure I take. I lastly want to thank my boyfriend, Charles Layman, who has constantly brought me tea and food while writing and has had insane amount of patience as I navigated my way through my Master's and my thesis.

TABLE OF CONTENTS

LIST OF TABLES

LIST OF FIGURES

LIST OF ABBREVIATIONS

ϵ	A symbol for permitivity
μ	A symbol for permeability
Ω	A symbol for ohms
ϕ	A symbol for phi
ρ	A symbol for rho
θ	A symbol for theta
cm	An abbreviation for centimeters
dB	An abbreviation for decibels
Hz	An abbreviation for Hertz
m	An abbreviation for meters
mm	An abbreviation for millimeter
PEC	An acronym for Perfect Electric Conductor
rad	An abbreviation for radians
RF	An acronym for Radio Frequency
S	An abbreviation for Siemens
TE	An acronym for Transverse Electric
TM	An acronym for Transverse Magnetic

CHAPTER 1: INTRODUCTION

1.1 Background of Metamaterials

Materials found in nature exhibit behaviors with certain properties such as Young's modulus, bulk modulus, mass density, permeability, and permitivity. These properties define how the materials behave such as stiffness in the case of Young's modulus or how conductive or magnetic the material is in the case of permitivity and permeability. The elements in the periodic table, shown in Fig 1.1, are the fundamental building blocks for materials and their properties. Unfortunately, there are limitations and restrictions to the behaviors of these materials that can be overcome with the use of metamaterials.

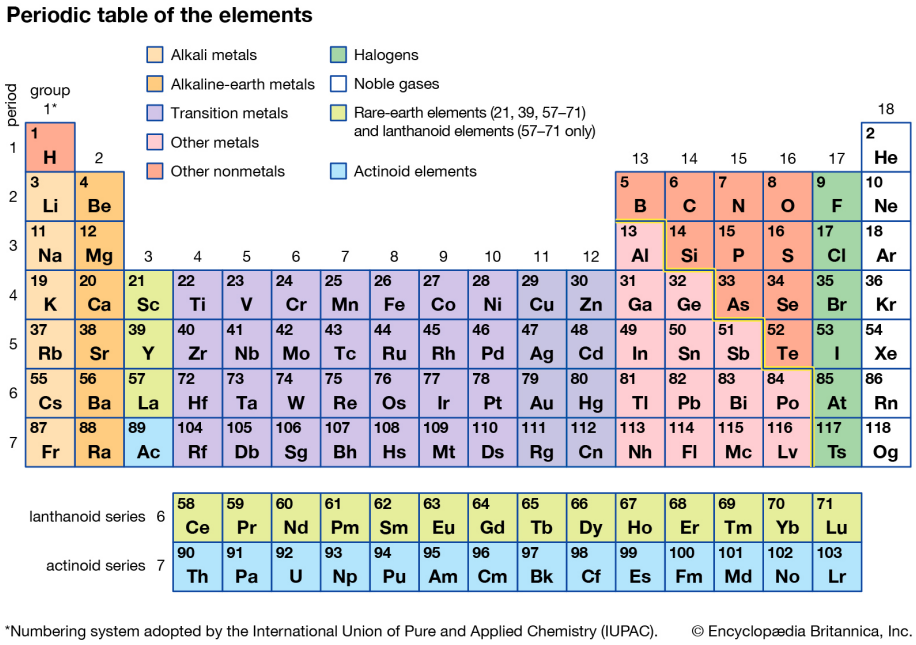

Figure 1.1: Periodic Table of Elements [1]

Metamaterials exceed the limitations of these properties and behaviors found in

nature through a host medium to create an effective bulk behavior that is able to exhibit unique properties. Through the composition, orientation, density, selection of host medium, geometry, and shape, a large number of applications ranging from thermodynamics and acoustics to mechanics and electromagnetism can be studied.

1.1.1 Thermodynamic Metamaterials

According to the laws of thermodynamics, a spontaneous process cannot be reversed and the spontaneity leads to an equilibrium process. The work done on a system to reach an equilibrium is expelled as heat [13]. In addition, since energy can neither be created nor destroyed, the energy ends up dispersing unless a metamaterial is introduced to take advantage of the laws of thermodynamics. Since the laws do not restrict how the process takes place in terms of time and space, the heat can be manipulated in a spatio-temporal behavior. A simple example of this is by restricting the flow of heat in one direction and concentrating it into another direction via anisotropic thermal metamaterials. Anisotropic materials are created through altering layers of two different mediums in which one has high heat conductivity and the other has low heat conductivity creating a "laminate." Laminates are typically used for thermal cloaking [3]. In [2], the structure of the laminate is exposed to a hot heat bath on one half and a cold heat bath on the opposite half to encourage the heat to flow from the hot side to the cold side. This method prevents an object from heating from the inside effectively cloaking the heat. The cloak makes the heat-flow distribution the same for both a homogeneous plate and the downstream side thus making the iso-temperature curves become vertical. The fabricated heat cloak is shown in Fig. 1.2.

Laminates can also be used for both thermal concentration, thermal inverting [14], and diffusion. Diffusion is currently being used for drug-delivery to make vesicles invisible to the immune system [15].

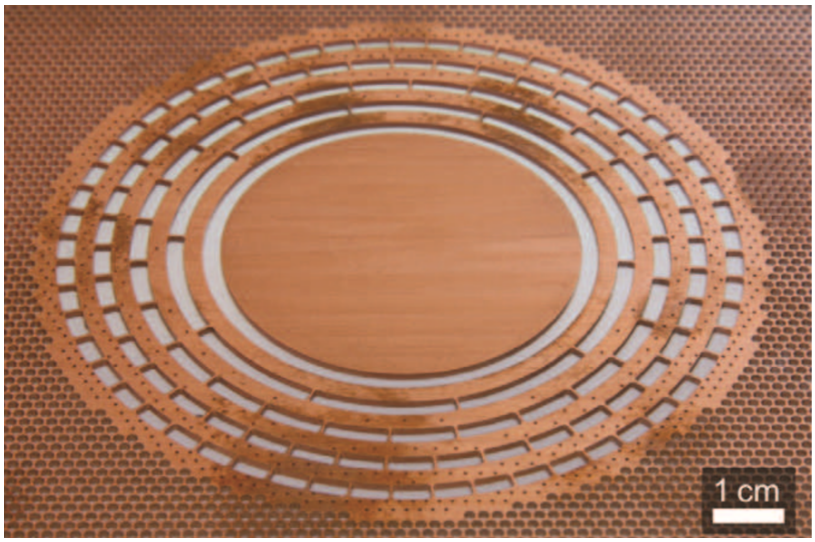

Figure 1.2: Example of fabricated thermodynamic heat cloak [2]

1.1.2 Acoustic Metamaterials

Acoustic waves naturally have positive phase velocities. Through manipulating sound waves to have a negative phase velocity and taking the negative phase velocity and mapping it to a fictitious coordinate system typically on an inhomogeneous and anisotropic material, cloaking in air and liquid can be performed. Acoustic metamaterials are analogous to electromagnetic metamaterials in the sense that the inverse of the bulk modulus corresponds to permitivity and mass density to permeability [3].

The first example ever tested of an acoustic metamaterial with a negative bulk modulus and negative mass density was performed with soft rubber spheres that were suspended in water. With the assumption that the finite shear of rubber is negligible, the rubber is treated to have a bulk modulus smaller than that of water resulting in low-frequency vibrational resonances. This relationship causes the rubber to shrink in frequencies below the resonance point and expand with frequencies above the resonance point along with a shift of 180^o. Since the mass density is related to the pressure, the bulk modulus becomes negative above the monopole resonance [16].

Acoustic metamaterials can also be created using hard-walled boundaries creating

pressure in order to slow down the wave. The normal component of the velocity with respect to the boundary's surface is zero at the surface [3]. This is accomplished through space-coiling in [4]. Using low-frequency ensures the wavelength to be long. The long wavelengths combined with unit cells that have thin, hard, solid plates forces the wave to propagate in a zigzag pattern as opposed to a straight line. The structure created by [4] is shown in Fig. 1.3 where the red "X" is a fluid channel that has a higher relative refractive index than the background fluid. The green structure is representative of the solid plates. By changing the liquid in the channel, the phase velocity of acoustic waves can be controlled.

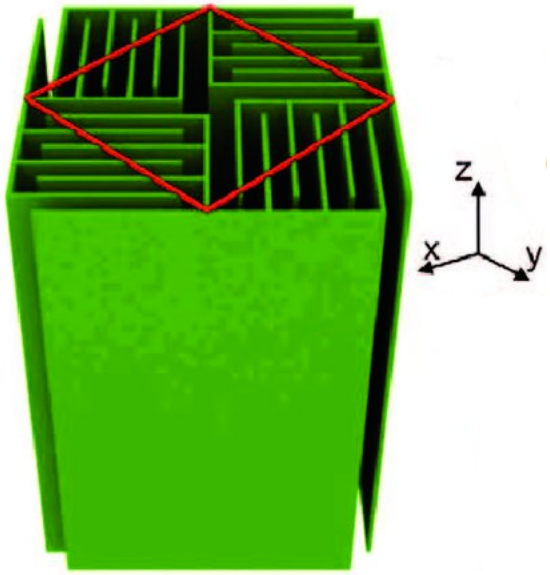

Figure 1.3: Four unit cells of a hard walled boundary acoustic metamaterial to control phase velocity by adjusting the liquid in the red square channel [3, 4]

The same concept of coiling the wave through space has also been accomplished for a two-dimensional airborne acoustic metamaterial and was fabricated through additive manufacturing to print thermoplastic walls [17,18]. The idea of space-coiling acoustic metamaterials for two-dimensional structures can be further extrapolated into a three-dimensional metamaterials as well [19].

The idea of using hard walled boundaries to create properties that are not natu-

rally occurring also can be applied to optics. In [20], a pair of periodically arranged perforated metal films are constructed into a fishnet design. The metal films are separated by a dielectric spacer and arranged in the normal direction. The metal film structure is designed to exhibit both negative magnetic permeability and negative electric permitivity around the resonance point of the design.

Another popular topic in metamaterials is the ability to cloak as seen in section 1.1.1. The idea of acoustic cloaking can be accomplished by manipulating the construction of Helmholtz resonators to control the effective phase velocity and impedance for a specific operational frequency [21]. An example of this is seen in [22] with a two-dimensional model in water through coordinate transformations that maps a point onto a circle. The Helmholtz resonators, machined into aluminum, help guide the pressure waves around the inner circle of the metamaterial effectively making the waves invisible. Recent advancements in technologies have expanded acoustic cloaking to be able to create a unidirectional free-space acoustic cloak in air that diminishes the scattering via the cloak and inner sphere. The experimental data proved to reduce scattering by a factor of ten [23].

1.1.3 Mechanical and Elastodynamic Metamaterials

There are a multitude of different types of mechanical and elastodynamic metamaterials in order to accomplish tasks that cannot be done with natural materials. For example, one desired material is one that is ultra lightweight, but also is stiff.

The mass density and stiffness, or Young's modulus, are typically positively proportionate, so making a naturally stiff material light weight is practically impossible [3]. Using stereolithography and electroplating with copper, [24] fabricated a mechanical metamaterial that had properties that had not previously been observed. The material changes the relationship of Young's modulus to static mass density from cubed to squared. The resulting material is so lightweight that air in the empty spaces of the material has comparable mass to the structure of the metamaterial.

When squeezing a sponge horizontally, the top and bottom of the sponge expands laterally due to its positive Poisson ratio. This behavior is common for isotropic elastic materials. An auxetic material opposes the common, natural behavior due to its negative Poisson ratio. Mechanical auxetic materials can also be intentionally anisotropic [3]. A naturally occurring anisotropic auxetic material is living bone tissue [25].

All rationally designed and fabricable auxetic metamaterials are based on a few motifs. As seen in Fig. 1.4 (a) the bow-tie structure is one of the motifs. The bow-tie structure contracts along the X and Z direction when pushed along the Z axis. The Poisson ratio magnitude and sign are controlled by the angle, α. The two-dimensional structure of the bow-tie can be constructed to perform as a three-dimensional metamaterial shown in Fig. 1.4 (b) [5].

Another motif to create auxetic mechanical metamaterials is a dilation element. [26] is researching materials to achieve an isotropic stable material with a Poisson ratio of -1. The unit cell has inner squares that rotate and the structure contracts along both orthogonal directions when pressure is applied to one side of the material. The rotation of the adjacent unit cells are opposite throughout the three-dimensional structure proven mathematically in [27]. As the limit of the thickness of the inner squares approach zero, the Poisson ratio also approaches -1.

Just like thermodynamic and acoustic metamaterials, mechanical metamaterials can also perform cloaking. A flexural wave is one that propagates in the xy plane, but has displacement on the thin membrane in the z direction. When the thickness of the membrane is significantly larger than the wavelength, bulk behavior is observed [3]. Through alternating concentric rings of effective small and large Young's modulus, a homogeneous material is constructed so the phase velocity is slowed down. This causes the azimuthal component of the cloak to be larger than the phase velocity. This was tested by exciting flexural waves with a loudspeaker creating back scattering

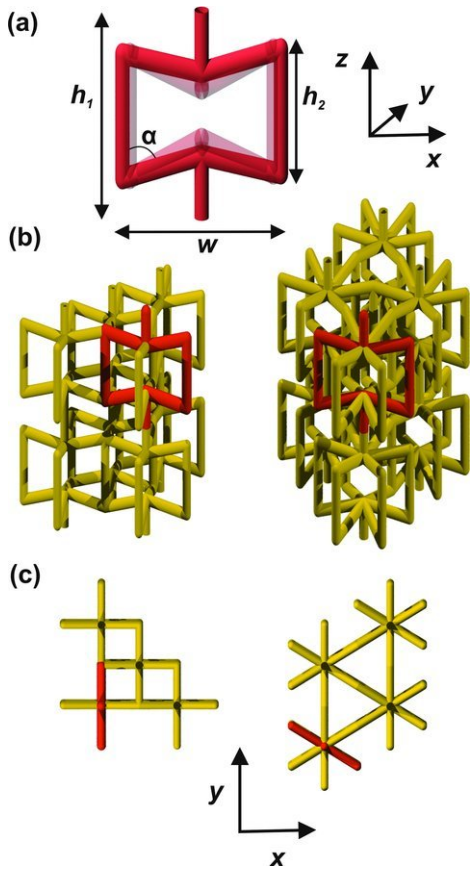

Figure 1.4: (a) Single bow-tie cell for a common type of auxetic material (b) Three-dimensional structure built by combining the singular cells shown in (a) (c) Top view of the three-dimensional structures shown in (b) [5]

and distortion. With the cloak applied, scattering and distortions were drastically reduced, but at high frequencies, the wavelength is not large enough to qualify as a bi-harmonic wave equation and the cloak loses its effectiveness [28].

There is an abundance of research currently in metamaterials to make cloaking a possibility for other fields in mechanics. For example, engineers are studying elastostatic cloaking using conformal coordinate transformations and a pentamode material [29]. A pentamode material, also called an anti-auxetic metamaterial, is one that deforms in six different ways where five of these deformations take practically zero force to accomplish. The last deformation supports one mode of a pentamode material [3]. In [30], the authors first suggested the idea of a pentamode material in

1995. Their design consisted of double-cone elements organized on a face-centered cubic translational lattice. Applying force to the metamaterial on all sides compresses the double-cone giving the structure a finite bulk modulus, but if any of the unit cells shears, the metamaterial falls apart. More recently, pentamode materials have been transformed into two-dimensional bi-mode materials through a honeycomb lattice shape [31, 32] or 'metal water' [33].

1.1.4 Electromagnetic Metamaterials

Electromagnetic metamaterials are comprised of electrically small unit cells to create a material that performs with a electromagnetic bulk behavior. A periodic array of conducting elements where the wavelength is comparably larger than the individual cell dimensions and lattice spacing can also create a medium with effective bulk behavior [6]. Veselago initially proposed the idea of negative permeability, μ, and permitivity, ϵ, in 1968 in [34]. He theorized that creating a medium with both negative μ and ϵ would introduce propagation characteristics that deviated from anything ever seen before such as a reverse Doppler shift, reverse Cherenkov radiation, and abnormal refraction. Refraction is where an electromagnetic wave is incident to a surface at an arbitrary angle and the direction of propagation is related to the refractive index and the materials the wave travels through and reflects off. The idea of refraction is used to design lenses and imaging [7]. A material with both negative μ and ϵ is classified as a 'left-handed' material. This type of material was not possible until Pendry *et.al* created a periodic array of nonmagnetic conducting cells to create a medium with a bulk behavior of magnetic permeability. At low frequencies, the effective μ proved to be very large, but at high frequencies, the material exemplified negative effective μ values [35]. Pendry used split ring resonators to accomplish these characteristics such as the one shown in Fig. 1.5 along with its resonance curve. The splits in the ring allows control over the resonant frequency wavelength to be much larger than the diameter of the rings. When the split-ring resonators are combined

in a periodic structure, strong magnetic coupling between unit cells is introduced creating an effective permeability.

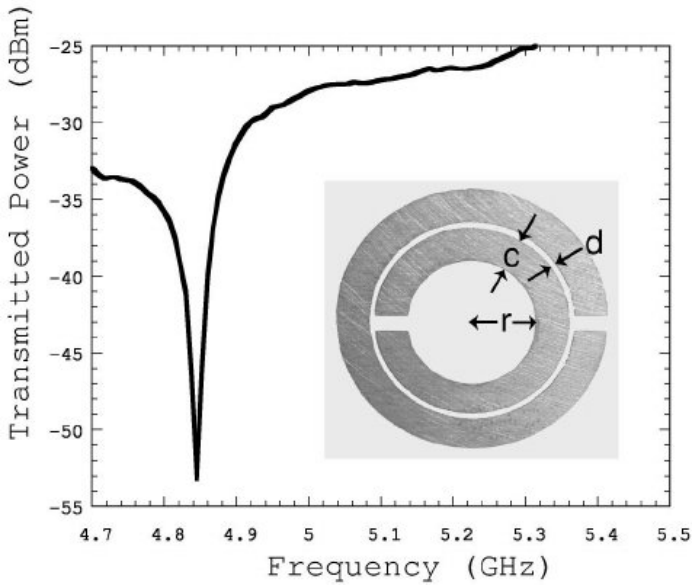

Figure 1.5: Split ring resonator to create negative effective μ and its corresponding resonance curve [6]

This same method of using split ring resonators to create a left hand material is seen in [7]. The structure, shown in Fig. 1.6, is a dimensionally periodic array of square split ring resonators with wires on the opposite side fabricated via shadow masking and etching techniques. This give the metamaterial properties of effective permeability, effective permitivity, and effective refractive index.

Similarly to metamaterials in the other fields, cloaking is a popular topic of research in electromagnetism commonly accomplished through coordinate transformations [36]. The coordinate transformation method excludes the interior fields of the penetrable object without effecting the external fields in theory making the interior fields appear invisible. This approach works for a media that is anisotropic with independently controlled μ and ϵ with relative magnitudes less than one. In turn, this limits the bandwidth to a small range of frequencies the metamaterial will be able to cloak [37]. The prospect of cloaking is still a relatively new research and the real-

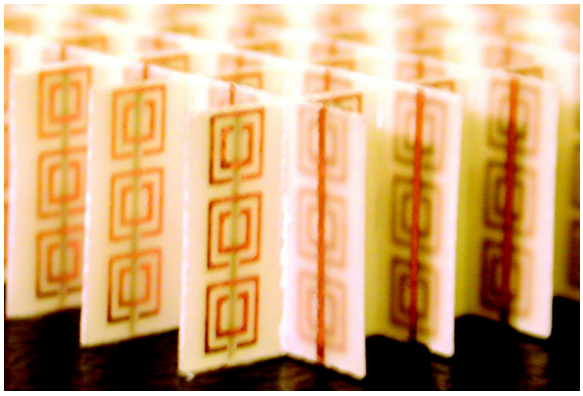

Figure 1.6: Square split ring resonators periodically arranged to perform as a left-handed material [7]

ization and ability of an electromagnetic cloak is discussed in [38]. Cummer explains how the metamaterial does not rely on system resonances or the dependence on the sign of μ and ϵ and how the derivations for a cloak are not unique. These factors will possibly allow small perturbations to the cloaking shell to not affect the cloaking abilities. Full-wave simulations for an electromagnetic cloak are explained in [38]. Conceptual cloaks are also being examined such as the space-time cloak [39]. This concept also uses a coordinate transformation that works in both space and time.

1.1.4.1 Disadvantages of Three-Dimensional Metamaterials

As discussed in section 1.1.4, the appeal of electromagnetic metamaterials is their ability of negative permitivity and permeability to create a negative refractive index [6, 7]. The ability to cloak using an anisotropic inhomogeneous metamaterial drew in lots of interest, but cloaking experimentally exhibited high loss and strong dispersion at the resonant frequencies and with the use of conductive materials. Fabrication of metamaterials also presented to be an issue. The construction of the materials tend to need micro and nano-fabrication which poses a feasibility of fabrication issue [40]. As an alternative, a metamaterial can be designed to be a planar structure, as opposed to three-dimensional, that can be fabricated with technologies that already exist such as lithography and nanoprinting methods. The ability to fab-

ricate the planar metamaterials, also known as a metasurface, is pushing the research away from three-dimensional metamaterials to metasurfaces. The thickness of the metasurfaces are typically sub-wavelength, thus a propagation constant is minimal making the effective permeability and permitivity of less importance. The focus on metasurfaces tends to be on modulated surface impedance and its ability to control aspects such as polarization, amplitude, and phase. Metasurfaces can also be implemented in various ways such as modulated surface impedance antennas and metascreens. Because metasurfaces are planar, the issue of loss from metamaterials is overcome using metasurfaces through the thinness of the planar structure and using the appropriate materials. In general, the issues encountered from three-dimensional metasurfaces and bulk behavior are overcome by metasurfaces while still providing sufficiently strong waves [41].

1.2 Motivation

The main application of metasurfaces and modulated metasurface antennas is for space due to the size and weight. Currently, satellites and other space technologies use reflectors or a phased array. Reflectors do not perform with a low profile and the phased arrays require a complex feeding system for reflection and transmission modules which can be costly and expel a large amount of energy. A modulated metasurface antenna is a alternative to other methods such as the reflectors or phased array due to its simple feeding mechanism, size, weight, cost, manufacturability, and customizability. In addition, it can be created to operate with specific electromagnetic characteristics to fulfill the requirements of varying designs. Typically metasurfaces are fabricated using printed circuit board technology. The two proposed metasurfaces in this thesis can be fabricated using a commercial 3D printer and use additive manufacturing to build the designs.

The first design presented is a modulated metasurface leaky wave antenna performing a surface wave transformation as shown in Fig. 1.7. As it propagates, it "leaks"

meaning all the power radiates upward at easily accommodated pointing angles with the ability to propagate both forward and backward. Modulated metasurface antennas began to grow in popularity after the Oliner and Hessel published their findings in [42]. Due to their flexibility and versatility in design, beam control, application to a magnitude of technologies, controllability of surface waves, controllability of aperture fields, and their characteristics of maintaining a low profile and low envelope of high gain antennas has drawn a lot of attention to the development of this technology [11, 43, 44]. In addition, the attractive properties of the modulated metasurface antennas makes it a appealing for space applications such as satellites for observing earth, space exploration, and the instruments used for data transmission [45,46]. Two different antenna designs are provided with one antenna being fully metallic and the other fully dielectric. The fully metallic form of the antenna can be utilized in harsher environments such as in space and earth observation and satellite communication [46]. In addition, with a low-loss conductive material, it can be additive manufactured in a laboratory setting. Since the antenna is fabricated of a metallic material, the antenna can be heavy and bulky. Thus, the fully dielectric modulated metasurface leaky wave antenna is presented to display the similarities of the performances for the two different material antennas. Unlike low-loss conductive filament, dielectric is low-cost, light, and easy to work with. Being able to create a fully dielectric antenna with additive manufacturing, an antenna with the same electromagnetic properties as the metallic antenna can be created, but at a lot cheaper price and a lot lighter weight. Being able to easily and cheaply make a modulated metasurface antenna with a commercial 3D printer makes the fabrication of this type of antenna easily accessible. In addition, the characteristics, such as the pointing angle, are easily adjustable allowing the design of the antenna to be easily manipulated to the desired application. The dielectric antenna also can be used in applications of satellite communication and wireless communication.

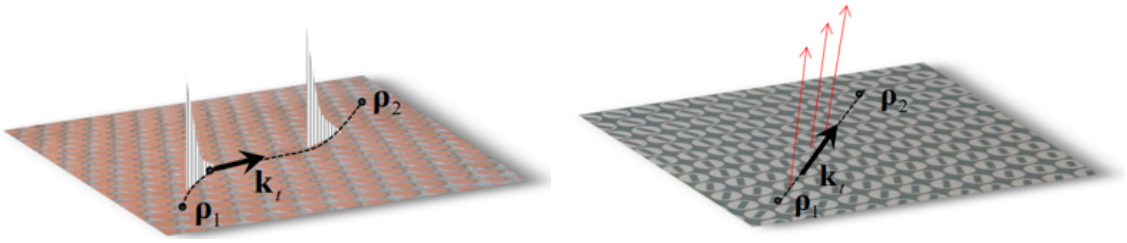

Figure 1.7: Wave being transformed as it propagates across the surface from the surface impedance

The second proposed metasurface is a polarization splitting metasurface through a space wave transformation. Two examples of space wave transformations are shown in Fig. 1.8 with the left showing a transformation of linear polarization to circular polarization and the right showing a beam steering effect. Most metascreens and metasurfaces currently published and researched are singularly polarized. To overcome this limitation, the metasurface presented is able to steer a beam at a predetermined angle dependent on the polarization. The impedance seen by a x-polarized wave is different than the impedance seen by a y-polarized wave thus creating different reflected angles from the screen. This technology can be incorporated into wireless communication, wireless tracking, imaging, and automotive radar.

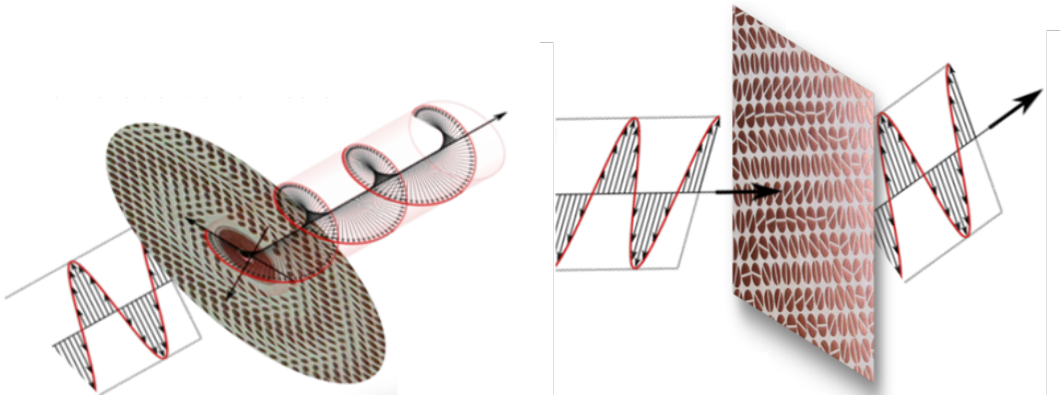

Figure 1.8: Left side shows a linearly polarized wave to a circularly polarized wave. The right shows a beam steering effect. Both show space wave transformations

1.3 Thesis Structure

The first chapter of this thesis covers a broad introduction into the field of metamaterials exploring different types amongst thermodynamics, acoustics, mechanical, and electromagnetism. This section also discusses some areas of improvement for metamaterials and how metasurfaces can fulfill those needs. The second section covers the motivation for the research for both the sinusoidally modulated metasurface metallic and dielectric antenna and the polarization splitting metasurface. The lasts section is the thesis structure.

Chapter 2 covers the design and analysis of metasurfaces starting with Floquet-Bloch theorem to solve periodic differential equations for both a one-dimensional and two-dimensional structure. The second section covers surface wave characteristics and analysis. Surface impedance characterization and surface wave dispersion characteristics are defined and examples are provided. The last section of the chapter is on modulated metasurfaces starting with impedance boundary conditions and how to find them. Next, isotropic and anisotropic metasurfaces are described and defined with mathematical derivations and examples.

Chapter 3 presents the process of the design and analysis of the sinusoidally modulated metasurface starting with a single unit cell. The process of creating an impedance to pin height database is discussed and exemplified with a linear case of modulation and a cylindrical modulation. The results are presented for a broadside antenna for both the metallic and dielectric antenna. The results are also presented for a non-broadside propagation for the metallic design and forward and backward propagation are shown to work with the dielectric antenna. Lastly, fabrication of this antenna is discussed using additive manufacturing and simulation results for the metallic printed antenna is provided.

Chapter 4 discusses the polarization splitting metasurface. The equivalent local transmission line model is presented along with the corresponding $ABCD$ matrix to

find the admittances of the screen for each polarization. A singular polarization of a beam being steered as it passes through the screen is exampled. This transitions to the dual polarization models and methods. The last section of this chapter discusses the optimization method that is used to find the different unit cell shapes to create a range of admittances. The last chapter presents the conclusions of this thesis.

CHAPTER 2: DESIGN AND ANALYSIS OF METASURFACES

Metasurfaces are planar metamaterials designed with sub-wavelength periodic unit cells with the ability to manipulate electromagnetic properties such as polarization, phase, and direction of propagation. Their properties of dispersion and reflection are utilized to create impedance surfaces imposing boundary conditions on the relationship between the tangential electric and magnetic fields. The impedance boundary conditions of the individual metasurfaces vary depending on their purpose, but they can either be isotropic or anisotropic. This chapter provides the analytical techniques required to solve periodic planar metasurfaces.

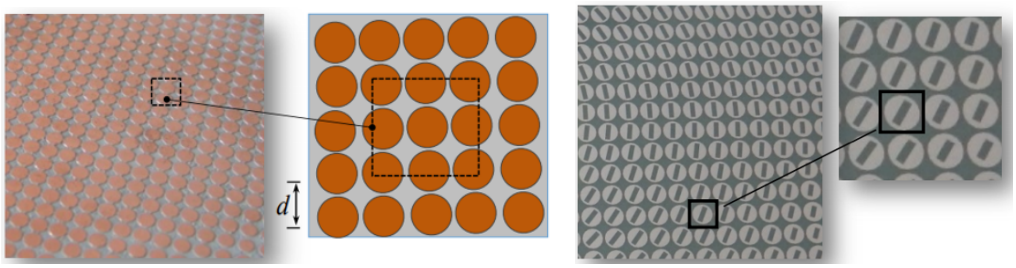

Figure 2.1: Local periodicity is assumed in order to simplify the analysis

In order to design the metasurfaces, a few assumptions need to be discussed in order to do the analysis. In order to solve for the fields and behaviors of how the metasurface will work, local periodicity is assumed. This means that unit cell geometry is assumed to be infinitely repeating in both the X and Y direction and their characteristics can be derived from the local geometry. Each patch in the metasurface can be seen such that it is embedded in a periodic metasurface simplifying the design a lot as shown in Fig. 2.1. Periodic Green's Function and the method of moments can be used to find the scattering and wave parameters and standard commercial software for a single

unit cell. Lastly, only the dominant Floquet modes are considered, which means n is equal to m is equal to zero in order to homogenize the fields and boundary conditions.

The first section of this chapter discusses the analysis of periodic structures through the Floquet-Bloch theorem. The second section describes surface impedance characterization and surface wave dispersion characteristics. The last section provides details explaining the difference between an isotropic and an isotropic modulated metasurface for impedance boundary conditions.

2.1 Floquet-Bloch Theorem

In the late 19^{th} century, mathematician Gaston Floquet published his research and derivation for solving one-dimensional differential equations with periodic coefficients [47]. A periodic structure is one that expands periodically in a defined direction with varying shape, size, and material. Almost fifty years later, Felix Bloch expanded Floquet's derivation to apply to three-dimensional systems specifically for electrons travelling across a periodic crystal lattice. Bloch explained the solution for a three-dimensional periodic function is the product of a plane wave multiplied by a periodic function that has an equivalent period to the lattice [48].

Consider an infinite structure that has a spatial periodicity, D_x, along the x axis of a Cartesian coordinate system with a wave vector for a plane wave defined as (k_x^i, k_y^i, k_z^i). The diffracted field originates with two generic sections defined by x_1 and x_2 where the difference of the two section, $x_1 - x_2$, is equal to nD_x. For a one-dimensional derivation, the relationship in the fields is only dependent on x conveyed in Eq. 2.1.

$$E(x_2) = E(x_1 + nD_x) = E(x_1)e^{-jk_x^i nD_x} \tag{2.1}$$

Equation 2.1 can be manipulated into a generic equation for a diffracted field as seen in Eq. 2.2

$$E(x) = E^{(\rho)}(x)e^{-jk_x^i x} \tag{2.2}$$

where $E^{(\rho)}(x)$ is equal to $E^{(\rho)}(x + nDx)$ for any integer, n. Consequently, for any integer multiple of D_x on the x axis, the boundary conditions for the diffraction problem are identical. The difference is only seen in the different phase factors when excited by an incident wave. According to Maxwell's equations and the properties of uniqueness, it can be assumed that the fields that are at these distances are the same and only differ from the same phase factor previously mentioned. Because of the properties of uniqueness for Maxwell's equation, the expression of $E^{(\rho)}(x)$ can be developed into a Fourier series expansion written as:

$$E^{(\rho)}(x) = \sum_{n=-\infty}^{\infty} E_n^{(\rho)} e^{j2\pi n \frac{x}{D_x}} \tag{2.3}$$

The coefficient of the Fourier series provided in Eq. 2.3 is expressed as:

$$E_n^{(\rho)} = \frac{1}{D_x} \int_0^{D_x} E^{(\rho)}(x)^{j2\pi n \frac{x}{D_x}} dx \tag{2.4}$$

Through substituting Eq. 2.3 into Eq. 2.2, the field for the periodic structure can be rewritten as:

$$E(x) = \sum_{n=-\infty}^{\infty} E_n^{(\rho)} e^{-j\left(k_x^i - \frac{2\pi n}{D_x}\right)x} \tag{2.5}$$

Equation 2.5 can be considered the summation of plane waves with a constant propagation along the x axis. Below, in Eq. 2.6, represents the spatial periodicity of a structure propagating along the x axis leading to a discretization of possible directions of propagation of re-radiated fields.

$$k_x = k_x^i - \frac{2\pi n}{D_x} \tag{2.6}$$

The spatial periodicity for a planar periodic structure, with a purely real wave vector, can help determine the direction of propagation for the transmitted and re-

flected waves shown in Fig 2.2. The figure shows a left and right hemisphere with rays equal to the wave number for the reflected wave, k_o^r, and the transmitted wave, k_o^t. The dashed lines in the figure are indicative of the periodic spacing. According to Maxwell's equations, the propagation vectors for Floquet modes must equate to the wave number in the medium it propagates through dictating the propagation vectors end at the curvature of the circle. Due to the limitations of Maxwell's equations and properties of uniqueness, the wave propagating along the x axis has its direction determined by Eq. 2.6.

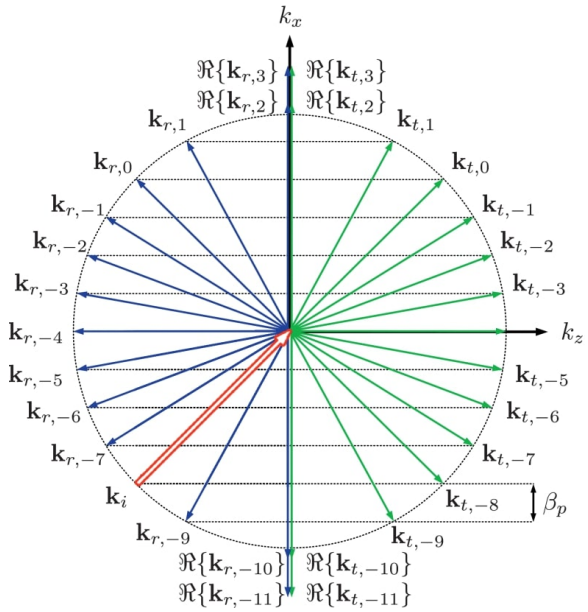

Figure 2.2: Spacial periodicity for a planar periodic structure [8]

The same concepts applied to the one-dimensional derivation of Floquet's theorem can be applied to both a two-dimensional and three-dimensional periodic structure. A two-dimensional version of the Floquet theorem applies to metasurfaces and three-dimensional derivation applies to metamaterials. Suppose a plane wave has a wave vector (k_x^i, k_y^i, k_z^i) and is incident on an infinite, impenetrable structure and is spatially periodic along x and y. The periodic variables are defined as D_x and D_y respectively. An example of a periodic structure in the x and y direction is shown in Fig. 2.3 where

the unit cell is clearly repeated in both directions [9].

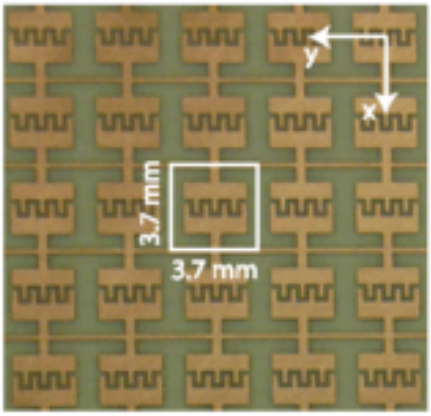

Figure 2.3: Example of a structure periodic along x and y [9]

Equation 2.2 can be expanded for a metasurface application as a function of electric field, E dependent of x, y, and z with the periodicity factors D_x and D_y with a phase dependence of k_x and k_y written as:

$$E(x, y, z) = E^{(\rho)}(x, y, z)e^{-j(k_x^i x + k_y^i y)} \tag{2.7}$$

Suppose a plane wave passes through a two-dimensional structure in free space at an angle. In order to solve this, periodic boundary conditions and port boundary conditions are imposed. The direction and polarization of the incoming and outgoing wave need to be defined to accurately solve the periodic analysis. Equation 2.7 can be expanded into its two-dimension Fourier series representation in Eq. 2.8.

$$E^{(\rho)}(x, y, z) = \sum_{n=-\infty}^{\infty} \sum_{n=-\infty}^{\infty} E_{nm}^{(\rho)} e^{j2\pi\left(n\frac{x}{D_x} + m\frac{y}{D_y}\right)} \tag{2.8}$$

The coefficients of the Fourier series expansion are:

$$E_{nm}^{(\rho)}(z) = \frac{1}{D_x D_y} \int_0^{D_x} \int_0^{D_y} E^{(\rho)}(x, y, z) e^{j2\pi\left(n\frac{x}{D_x} + m\frac{y}{D_y}\right)} dxdy \tag{2.9}$$

Through substituting Eq. 2.8 into Eq. 2.7, the field can be represented as:

$$E(x,y,z) = \sum_{n=-\infty}^{\infty} \sum_{n=-\infty}^{\infty} E_{nm}^{(\rho)} e^{-j(k_{xn}x + k_{ym}y)} \tag{2.10}$$

where the wave numbers for x and y are:

$$k_{xn} = k_x^i - \frac{2\pi n}{D_x} \tag{2.11}$$

$$k_{ym} = k_y^i - \frac{2\pi m}{D_y} \tag{2.12}$$

The electric field defined in Eq. 2.10 must satisfy the Helmholtz equation derived from Maxwell's equations where k is the wave number of the medium.

$$\nabla^2 E + k^2 E = 0 \tag{2.13}$$

By replacing Eq. 2.10 into Eq. 2.13, the equation becomes:

$$\sum_{n=-\infty}^{\infty} \sum_{m=-\infty}^{\infty} \left[\frac{\delta^2}{\delta z^2} E_{nm}^{(\rho)}(z) - k_{xn}^2 E_{nm}^{(\rho)}(z) - k_{ym}^2 E_{nm}^{(\rho)}(z) + k^2 E_{nm}^{(\rho)}(z) \right] = 0 \tag{2.14}$$

Rewriting the equation through combining constant terms and substituting a variable to represent the wave numbers, the equation is simplified to:

$$\sum_{n=-\infty}^{\infty} \sum_{m=-\infty}^{\infty} \left[\frac{\delta^2}{\delta z^2} E_{nm}^{(\rho)}(z) + k_{znm}^2 E_{nm}^{(\rho)}(z) \right] = 0 \tag{2.15}$$

$$k_{znm}^2 = k^2 - k_{xn}^2 - k_{yn}^2 \tag{2.16}$$

Taking the solution of the wave equation in square brackets in Eq. 2.15 yields:

$$E_{nm}^{(\rho)}(z) = E_{nm}^{(\rho 0)} e^{-jk_{znm}z} \tag{2.17}$$

where $E_{nm}^{(\rho 0)}$ is a constant. Substituting Eq. 2.17 into Eq. 2.10 brings the final expression of the electric field of a two-dimensional periodic structure shown in Eq. 2.18.

$$E(x,y,z) = \sum_{n=-\infty}^{\infty} \sum_{m=-\infty}^{\infty} E_{nm}^{(\rho 0)} e^{-j(k_{xn}x + k_{um}y + k_{znm}z)} \tag{2.18}$$

The n and m terms dictate the Floquet modes of the spatial harmonic wave. When both n and m are equal to zero, the fundamental Floquet mode is being excited. Eq. 2.18 conveys that the diffracted electric field for a two-dimensional periodic structure is the infinite sum of Floquet modes. In cases where the squares of the wave vector in x and y added are less than the wave number squared, Eq. 2.19, the z component of the wave vector will be real.

$$k_{xn}^2 + k_{ym}^2 \leq k^2 \tag{2.19}$$

The z component of the wave vector when real can be written as:

$$k_{znm} = \sqrt{k^2 - k_{xn}^2 - k_{ym}^2} \tag{2.20}$$

When Eq. 2.20 is real, the harmonics are traditional planes waves and are considered to be homogeneous and non-evanescent. Since the result is a plane wave, the phase is constant across the entire wave. In addition, because the wave is homogeneous, the amplitude is also constant through the plane perpendicular to the direction of propagation. Oppositely, the sum of the squares for the x and y component of the wave vector can become larger than the wave number of the medium shown in Eq. 2.21.

$$k_{xn}^2 + k_{ym}^2 > k^2 \tag{2.21}$$

The results of this is that the wave vector for z becomes completely imaginary:

$$k_{znm} = -j\sqrt{k^2 - k_{xn}^2 - k_{ym}^2} \tag{2.22}$$

When the z component of the wave vector is purely imaginary, the wave is considered to propagate with evanescent modes. These waves propagate orthogonal to a surface with constant phase. The magnitude of these waves also decrease exponentially orthogonal again to a constant width surface. Without losses, the wave propagates in the xy plane and attenuates along z. These types of evanescent waves are commonly used for the design of metasurfaces.

2.2 Surface Wave Characteristic and Analysis

This section discusses surface wave characteristics and analysis. The first part of this section provides details on the characterization of surface impedance. The latter half of the section talks about equivalent circuit theory to create a dispersion diagram for a surface wave.

2.2.1 Surface Impedance Characterization

An electromagnetic wave bound to an interface between two different materials is considered a surface wave. The surface impedance of a metal surface can be manipulated by adding texture to control the surface wave properties such as determining if the surface is inductive or capacitive, magnitude, and phase. Consider a surface with an impedance Z_s with an attenuation constant, α shown in Fig. 2.4.

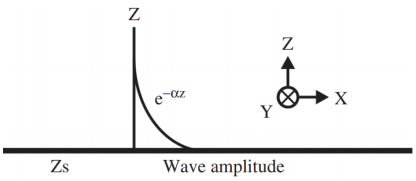

Figure 2.4: Surface wave attenuating in the z direction with an attenuation constant, α [10]

Through Maxwell's equations applied to the surface impedance in relation to surface waves, transverse magnetic (TM) waves are shown to occur on inductive surfaces expressed as:

$$Z_{s,TM} = \frac{j\alpha}{\omega\epsilon} \tag{2.23}$$

Oppositely, transverse electric waves (TE), occur on capacitive surfaces expressed as:

$$Z_{s,TE} = \frac{-j\omega\mu}{\alpha} \tag{2.24}$$

In both equations, μ and ϵ are the permeability and permitivity respectively and ω is the angular frequency. In addition, both equations are considered purely reactive and respect Foster's theorem. TE waves are electromagnetic waves that have electric field transverse to the propagating wave. For example, a wave propagating in the x direction would have field in the y direction. A TM wave is the same concept, except the wave has a magnetic field in the transverse direction of propagation [10].

2.2.2 Surface Wave Dispersion Characteristic

For a metasurface, as previously discussed, the surface acts as an effective medium when the unit cells are very small in comparison to the wavelength. If the metasurface is designed with metallic patches that have narrow spaces, the effective impedance appears capacitive. If a current oscillates between neighboring patches, the impedance becomes inductive. Oftentimes, the surface has both capacitive and inductive elements and can be modeled using a parallel LC resonant circuit. Consequentially, the impedance of the surface can be modeled as:

$$Z_s = \frac{j\omega L}{1 - \omega^2 LC} \tag{2.25}$$

Figure 2.5(a) pictorially describes the capacitive coupling behavior with the capacitor

notated by the C and the positive and negative symbols in the gap of the circuit. The current loop creating inductance is also shown using the circular arrow with an inductor value L. Figure 2.5(b) is the symbolic circuit to represent the behavior of the metasurface and the top half of the figure.

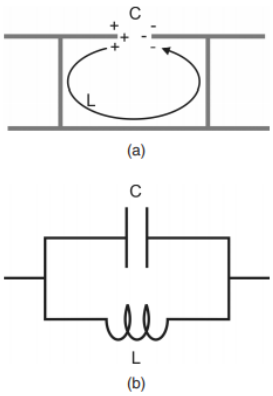

Figure 2.5: LC circuit representation of a metasurface [10]

The resonant frequency, ω_0, is thus $1/\sqrt{LC}$. From Eq. 2.25, the surface is inductive below the resonant frequency which supports TM waves and the surface is capacitive above the resonant frequency supporting a TE wave. As frequency approaches a resonant value, the impedance approaches becoming purely real and a surface wave is not supported.

To describe the impedance surfaces, an effective surface impedance model is used. The approach of using an equivalent lumped element circuit is only valid when the unit cells are much much smaller than the wavelength. This model is used to predict the reflection properties. The dispersion relation is described as:

$$k^2 = \mu_0 \epsilon_0 \omega^2 + \alpha^2 \tag{2.26}$$

In the above equation k is the wave number, μ_0 is the free space permeability, ϵ_0 is the free space permitivity, ω is the radial frequency, and α is the attenuation constant or sometimes called the decay constant.

Through combining Eq. 2.23 and Eq. 2.26, the wave number can be expressed as a function of the radial frequency and free space impedance for a TM wave where c as the speed of light in a vacuum.

$$k_{TM} = \frac{\omega}{c}\sqrt{1 - \frac{Z_s^2}{\eta^2}} \tag{2.27}$$

The same concept can be applied to a TE wave by combining Eq. 2.24 and Eq. 2.26.

$$k_{TE} = \frac{\omega}{c}\sqrt{1 - \frac{\eta^2}{Z_s^2}} \tag{2.28}$$

Substituting Eq. 2.25 into both Eq. 2.27 and Eq. 2.28, the dispersion diagram is created. An example of a dispersion diagram is provided in Fig. 2.6. The resonant frequency is marked by an f_0 making it obvious that TM modes are supported below the resonance point and TE waves are supported for frequencies above the resonance. Also note, at the lower end of the dispersion curve, the waves are close to the light line and not strongly bound to the surface, but as the frequency increases, the curves bend away from the light line and become more strongly bound to the surface.

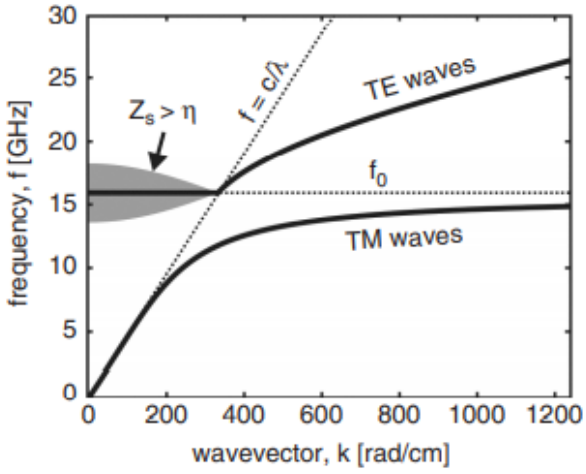

Figure 2.6: Example of a surface wave dispersion diagram for a surface with C=0.05 pF and L=2 nH [10]

The model described above helps predict electromagnetic properties such as beam shape, polarization, and the reflection phase.

2.3 Modulated Metasurfaces

Modulated metasurfaces are designed based on their impedance boundary conditions. This sections describes what an impedance boundary condition is in relation to Maxwell's equations. Isotropic and anisotropic boundaries are explained theoretically, derived mathematically, and examples are provided to show their difference.

2.3.1 Impedance Boundary Conditions

Metamaterials and metasurfaces use scattering of waves in a medium in order to achieve the desired characteristics, but modeling this can be difficult since the field expands both inside and outside of the scattering material. Since the field scatters three-dimensionally, volume integrals would be required to solve for the fields. If an electromagnetic wave is incident on a surface, the analysis can be simplified to surface area integrals through incorporating impedance boundary conditions [49]. Impedance boundary conditions relates the tangential components of the electric and magnetic field using an impedance factor that is a function of the surface properties, such as capacitance or inductance, and the incident field.

When the electromagnetic wave interfaces between two non-perfectly conducting isotropic homogeneous mediums is considered an exact boundary condition. Under these conditions, the cross product of normal vector to the electric field and the normal vector to the magnetic field equals to zero at the surface. Also, the dot product of the normal vector to the electric field density and the normal vector dotted with the magnetic field density is also equal to zero at the surface. These properties are not independent of each other and thus create an impedance boundary condition. This method relates the first medium to the second medium. When the second medium is a perfect electric conductor (PEC), only the fields in free space or dielectric are

considered. This changes the initial conditions of this type of boundary condition to:

$$\hat{n} \times E = 0 \tag{2.29}$$

$$\hat{n} \cdot B = 0 \tag{2.30}$$

$$\hat{n} \cdot D = \delta \tag{2.31}$$

$$\hat{n} \times H = K \tag{2.32}$$

where δ is the charge distribution and K is the current distribution. If the refractive index of the PEC is large compared to free space, Eq. 2.29 and Eq. 2.30 will be the only fields that appear in free space [50]. The way to instruct the local characteristics of a metasurface is by studying the scattering from an infinite two dimensional dielectric slab as shown in Fig. 2.7. This structure is analogous to a transmission line with the top part of the model representing air and the dielectric slab representing the dielectric in the transmission line.

2.3.1.1 Isotropic Modulated Metasurfaces

Assume a uniform impedance boundary with a uniform inductive reactance making it considered isotropic for a cylindrically modulated surface. Since the reactance is inductive, the type of fundamental wave being excited is TM as explained in section 2.2.1. This also dictates that the relationship between the tangential components of the electric field and the tangential components can be expressed as:

$$jX_s z \times (H \times z)|_{z=0} = E \times z|_{z=0} \tag{2.33}$$

where X_s is a positive scalar value. The tangential electric and magnetic surface waves are defined as:

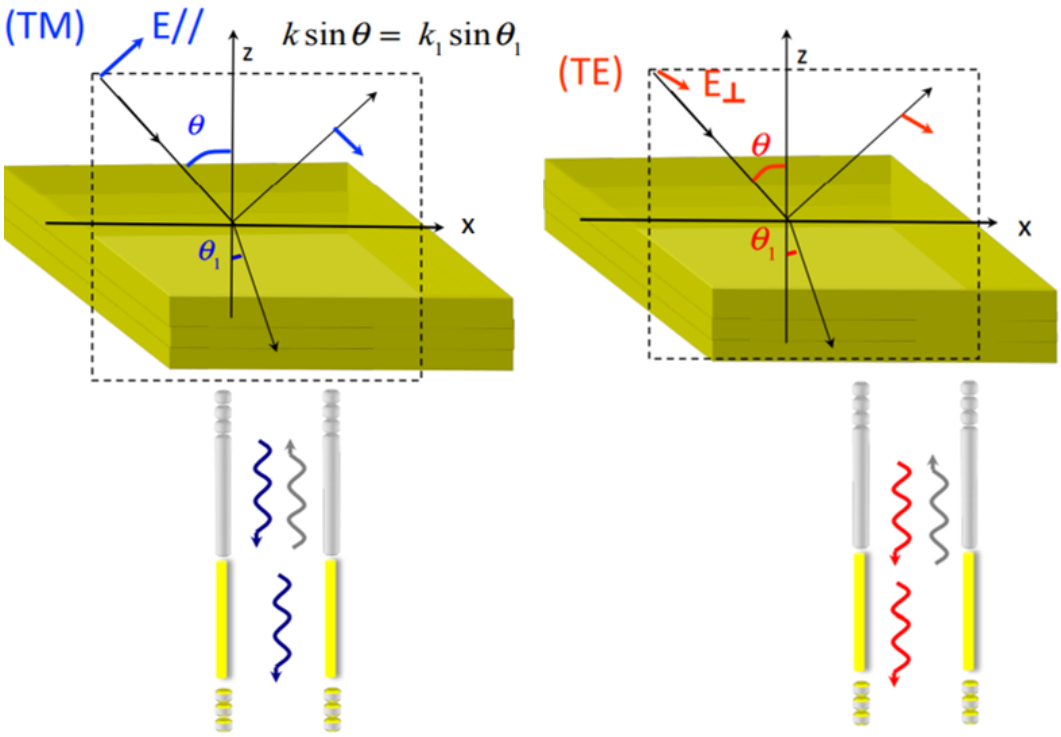

Figure 2.7: Two dominant mode for an incident wave on a dielectric slab analogous to a transmission line

$$E_{sw}^{tan} = I_{TM} j X_s H_1^{(2)}(\beta_{sw}\rho)\hat{\rho} \tag{2.34}$$

$$H_{sw}^{tan} = -I_{TM} X_s H_1^{(2)}(\beta_{sw}\rho)\hat{\Phi} \tag{2.35}$$

where I_{TM} is the current, X_s is the impedance, β_{sw} is the phase constant of the surface wave, $H_1^{(2)}$ is the first order Hankel function of the second kind, and the $\hat{\rho}$ and $\hat{\Phi}$ are components of a radial coordinate system. The phase constant of the surface wave can be found by imposing a resonance for a free space propagating TM mode wave:

$$\beta_{sw} = k\sqrt{1 + \left(\frac{X_s}{\zeta}\right)^2} \tag{2.36}$$

If metallic periodic cladding is added to the dielectric slabs in Fig. 2.7, a surface impedance is added to the transmission line model modeled in Fig. 2.8. A surface

is considered isotropic if the geometry of the cells that make up the surface are symmetric with respect to the direction of propagation of the supported mode.

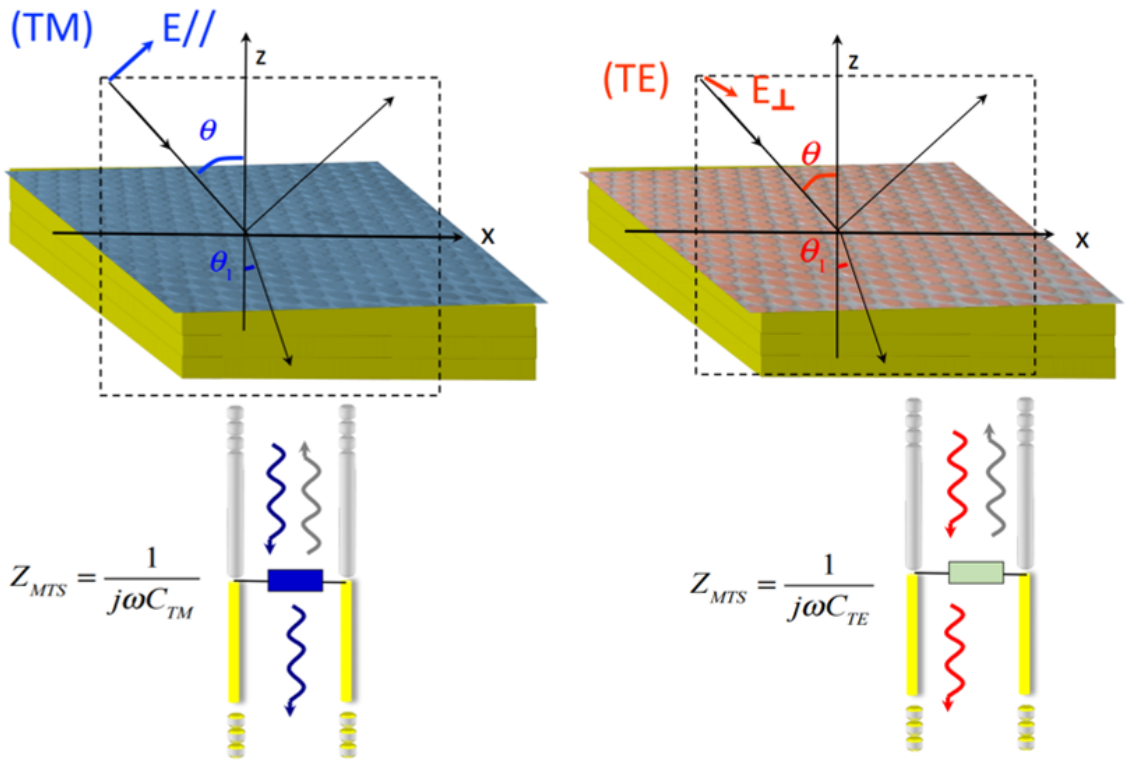

Figure 2.8: Periodic cladding added to the infinite dielectric slab creating an isotropic surface impedance

An example of this type of isotropic surface impedance is shown in Fig. 2.9. The periodic PEC square and circle patches on a grounded slab are symmetric to a circularly polarized wave. Another thing to note is that the individual unit cells are small in comparison to the wavelength of the operating frequency.

To create a modulated impedance, each cell is designed for a specific value of impedance in turn making the overall impedance of the surface appear to modulate as a smooth, continuous impedance expressed as a scalar, X_s. Since this is a scalar, the relationship of the tangential components of the electric and magnetic field is equal to $jX_s(\rho)$.

For both transverse electric and transverse magnetic waves, the amplitude of the transverse wave vector is $k_t = k_t(\rho)\hat{k}_t(\rho)$. The dispersion equation for an isotropic

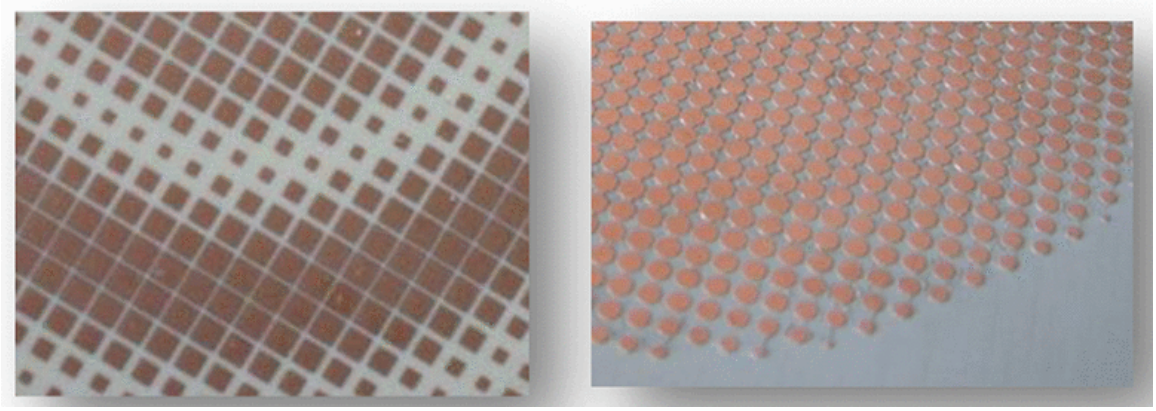

Figure 2.9: Two examples of metasurfaces with isotropic boundary conditions [11]

impedance can be expressed through the transverse resonance method below.

$$k_{tn}(\rho) = k\sqrt{1 + \left(\frac{X_s(\rho)}{\zeta}\right)^2} \tag{2.37}$$

where k is the wave number of the medium and ζ is the impedance of free space. Equation 2.37 shows that when k_{tn} is greater than the free space wave number, the fields attenuates exponentially normal to the metasurface shown in Fig. 2.10 with the spiral pattern indication the pattern of the impedance.

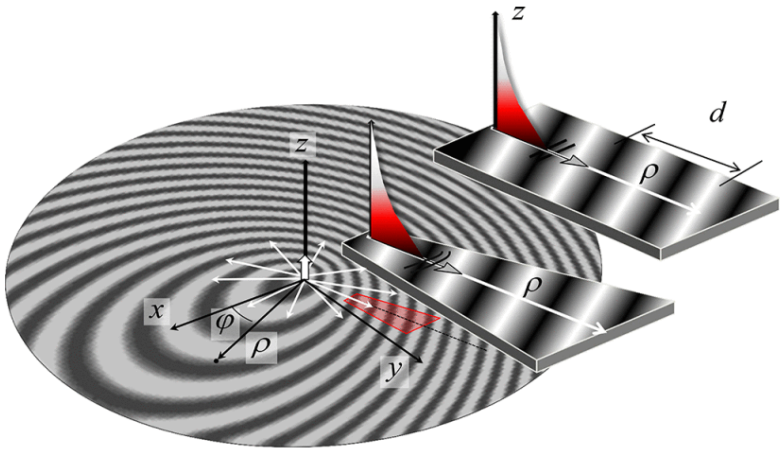

Figure 2.10: Field attenuating exponentially normal to a metasurface with a spiral pattered impedance [11]

The modulation of the wave vector obtained through a modulated surface impedance

produces a change in the phase velocity and the path of propagation for the surface wave supported by the metasurface. This is done through the imposed boundary conditions that will increase or decrease k_t locally in order for the wave to follow the changing impedance. The propagating wave path is thus defined by the local refractive index and invoking the Fermat principle of a wave taking the minimum optical path.

2.3.1.2 Anisotropic Modulated Metasurfaces

An anisotropic impedance boundary condition is created when the tangential fields on the surface are $E_{sw}|_{z=0^+} = Z \cdot (z \times H_{sw})|_{z=0^+}$. An anisotropic boundary condition implies that the impedance is a tensor that relates the tangential electric field to the tangential magnetic field. The TE and TM modes are coupled because the impedance is anisotropic illustrated in Fig. 2.11.

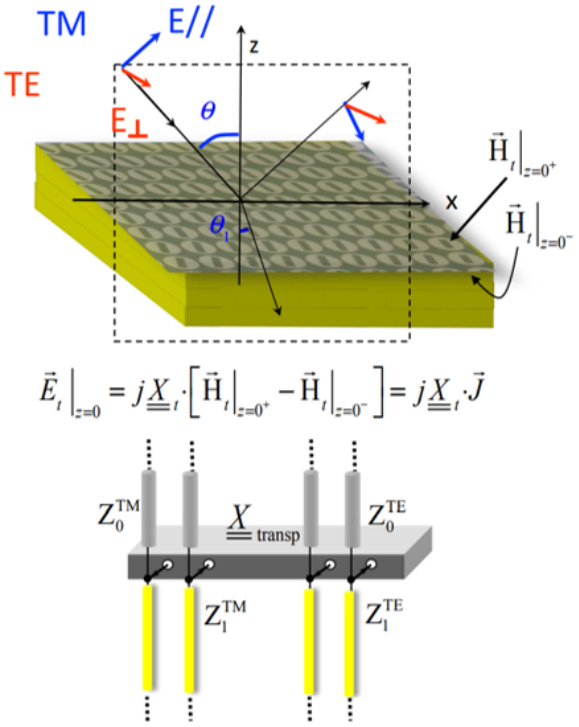

Figure 2.11: Anisotropic surface impedance on an infinite dielectric slab showing the TE and TM coupling effect

The way to design an anisotropic surface is to create a shape that is not symmetric to the surface wave propagation. Four different examples of this are exhibited in Fig. 2.12 with the arrow designating the direction of incident wave [51].

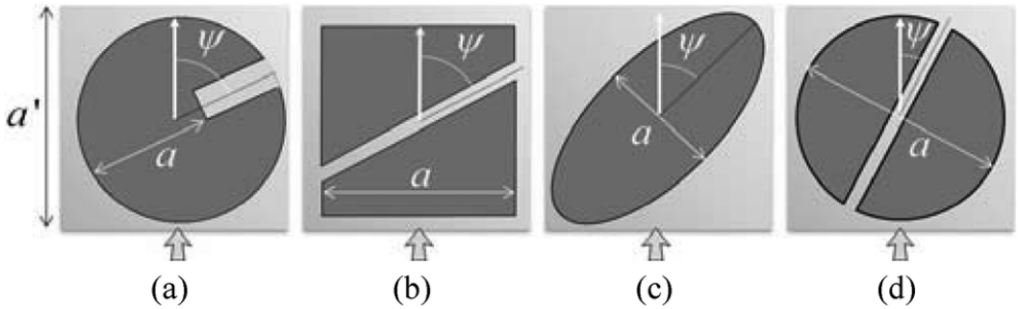

Figure 2.12: Four different examples of unit cells to create an anisotropic boundary conditions with arrows indicating the direction of incident wave [12]

The unit cells in Fig. 2.12 are designed based on two specific non-dimensional parameters labeled as Ψ and a and a' related as a/a'. These two variables are used to create the impedance profile for the metasurface. The important thing to note about these unit cells is that the incident wave direction changes the impedance of the unit cell making it considered anisotropic.

CHAPTER 3: SINUSOIDALLY MODULATED METASURFACE ANTENNAS

This chapter will discuss the design and analysis of a two-dimensional isotropic modulated metasurface antenna. The first section describes the process for a one-dimensional modulation along x and how to create an impedance to height database using an eigenmode simulation. The second section expands the one-dimensional modulation to a two-dimensional modulation dependent on ρ and ϕ. The results are provided for a metallic and dielectric broadside design. The following section demonstrates the versatility of the antenna by providing the results of three different pointing angles with one of the angles being backward radiation. The last section discusses the process of fabrication for both the metallic and dielectric antennas.

3.1 Synthesis and Design

Assume a modulated surface with an average inductance defined as X_{av} to support the propagation of a transverse magnetic (TM) surface wave. The wave number for this wave can be expressed as:

$$\beta_{sw} = k\sqrt{1 + \left(\frac{X_{av}}{\zeta}\right)^2} \tag{3.1}$$

where k is the free space wave number and ζ is the free space impedance. A sinusoidal modulation can be applied to this surface. For a one-dimensional modulation, the impedance of the surface is described in Eq. 3.2. For this equation, the surface wave propagates along the x axis with the modulation factor notated as M and d is the period of modulation.

$$X_s(s) = X_{av}\left[1 + M\sin\left(\frac{2\pi x}{d}\right)\right] \tag{3.2}$$

The transverse to z wave number for an n-indexed Floquet mode expansion is provided below:

$$k_{tn} = \beta_{sw} + \beta_{\Delta} - j\alpha + \frac{2\pi n}{d} \tag{3.3}$$

β_{Δ} is the perturbations in the phase constant and α is the perturbations in the attenuation constant caused from modulation. If $M = 0$, there are no perturbations and β_{sw} accurately describes the transverse wave number, k_t. If the real part of the transverse wave number, $k_{t,n}$ is less than the free space wave number, k, the surface wave becomes a leaky wave. The dominant mode of the leaky wave occurrs when the refractive index, n, is equal to -1 thus producing a radiation in the direction given by:

$$\beta_{sw} + \beta_{\Delta} - \frac{2\pi}{d} = k \sin\theta_o \tag{3.4}$$

where θ_o is the angle with respect to the z-axis. Through plugging Eq. 3.1 into Eq. 3.4 and ignoring the effects of the phase constant perturbations, the period of a singular forward beam can be defined as shown in Eq. 3.5. Considering the waves are propagating in free space, the equation is able to be simplified and written with a dependence on wavelength.

$$d = \frac{2\pi}{k} \frac{1}{\sqrt{1 + \left(\frac{\hat{X}}{\zeta}\right)^2} - \sin\theta_o} = \frac{\lambda}{\sqrt{1 + \left(\frac{\hat{X}}{\zeta}\right)^2} - \sin\theta_o} \tag{3.5}$$

Eq. 3.5 is accurate when $\hat{X}/\zeta > \sqrt{4\sin\theta_o(1 + \sin\theta_o)}$. For frequencies below 100 GHz, the impedance modulation can be achieved through the design of individual unit cells that are substantially smaller than the wavelength to acquire the desired properties. For frequencies in the terahertz range, losses in a dielectric can pose an issue. Both a fully metallic and a fully dielectric antenna are presented in this chapter with an

operational frequency of 15 GHz so results can be compared.

To create a database in order fulfill the modulation range in a period from Eq. 3.2, a square unit cell with sides, a, is created with a cylindrical pin inside with an arbitrary radius that is able to cover the entire database of impedance for a modulation. Figure 3.1(a) shows a metallic pin with a radius of 0.35 mm and Fig. 3.1(b) shows a dielectric pin with a radius of 1.35 mm inside an air box. To gather the dimensions of the unit cell and modulation period, θ_o is equated to 1^o. For one period, there are six pins making the period of modulation, d, 16.61 mm and the individual unit cell size 2.77 mm from Eq. 3.5 and dividing it by the number of unit cells per period. Notice the radius of the dielectric pin is much larger than the metallic pin in order to reach the desired impedance range. The dielectric pin is only able to reach the required values of impedance when the diameter of the pin is close to the size of the unit cell. The permitivity of PEC is infinite, but the permitivity of a dielectric is a lot smaller requiring a lot more material in order to carry the surface wave.

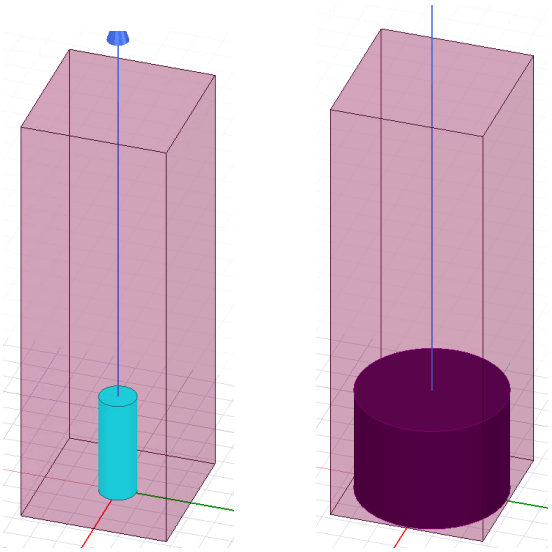

(a) Metallic pin (b) Dielectric Pin

Figure 3.1: Unit cells for the metallic and dielectric antenna in a tall air box used in an eigenmode simulation to find corresponding impedance to the height of the pin

To be able to construct an accurate database of heights to match impedance, a

range of heights is swept across a phase range of $10^o - 175^o$ using the simulation software Ansys High Frequency Structure Simulator (HFSS). Phase below 10^o produces non-useful data because it is too close to the light line. Since the structure is periodic, the phase is stopped right before 180^o. Local periodicity is assumed and periodic boundaries are applied to the unit cell. To ensure no complex Floquet modes are introduced, the height of the air box is always at least three periods taller than the pin. For the metallic pin, the results of the first three modes of the eigenmode simulation when the pin height is 1 mm is provided showing the relationship between the phase and frequency. Figure 3.2 shows the first mode in a red, solid line, the second mode in a blue, dashed line, and the third mode in a green, dotted line.

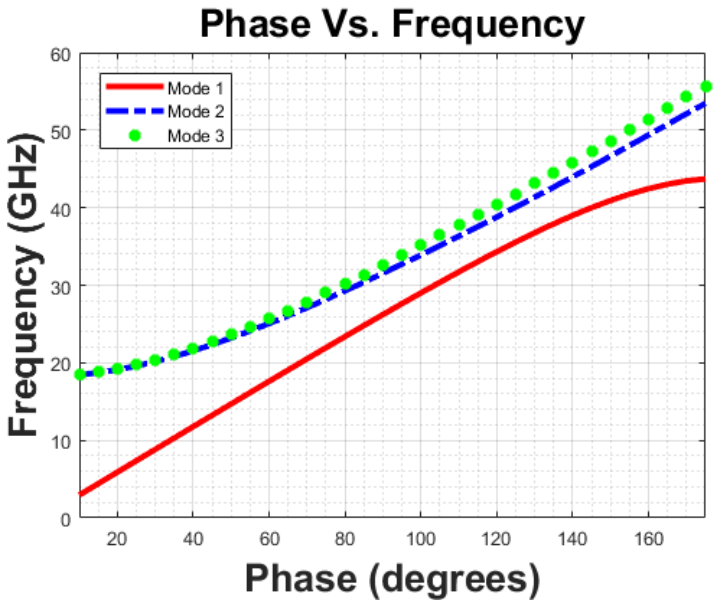

Figure 3.2: Phase versus frequency for an eigenmode solution for a metallic pin with radius of 0.35 mm and a unit cell size designed with θ_o. The first Floquet mode is a red, solid line, the second mode is a blue, dashed line, and the third mode is a green, dotted line

The dispersion of the wave for the first Floquet mode of a metallic pin with a height of 1 mm is shown with a solid, red line in Fig 3.3 compared against the light line in a dashed, blue line. The plot is indicative of the broadside metallic design.

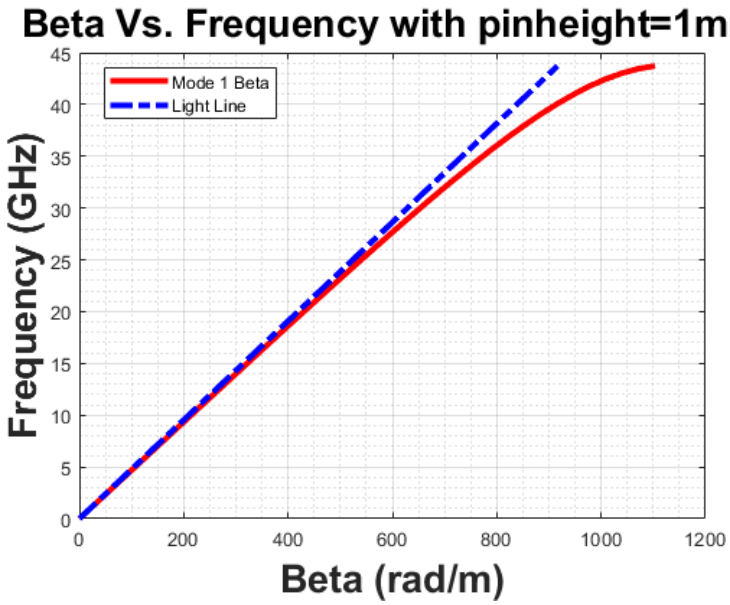

Figure 3.3: Beta versus frequency with the dispersion of the wave for the first Floquet mode of a metallic pin with a height of 1 mm is shown with a solid, red line against the light line in a dashed blue line for comparison

A transverse resonance condition is applied between jX and the free space TM impedance to obtain Eq. 3.6.

$$X = \zeta \frac{\sqrt{\beta_{sw}^2 - k^2}}{k^2} \tag{3.6}$$

Using the above equation, the varying β_{sw} for the different heights are utilized to find the corresponding impedance for different heights of pins. The black dots in Fig. 3.4 are indicative of the values of impedances collected from the simulation using Eq. 3.6 for the varying heights. The red line is the interpolated values for the heights to match the impedances for the metallic setup and the blue line is the interpolated heights for the dielectric pin. Notice the required height range for the dielectric is a lot larger to cover the range of impedances than the range for the metallic pins. Again, this is due to the low value of the permitivity of the dielectric.

Equation 3.2 is plotted and shown as the magenta line in Fig. 3.5 displaying one period of impedance for a one-dimensional sinusoidal modulation with a modulation

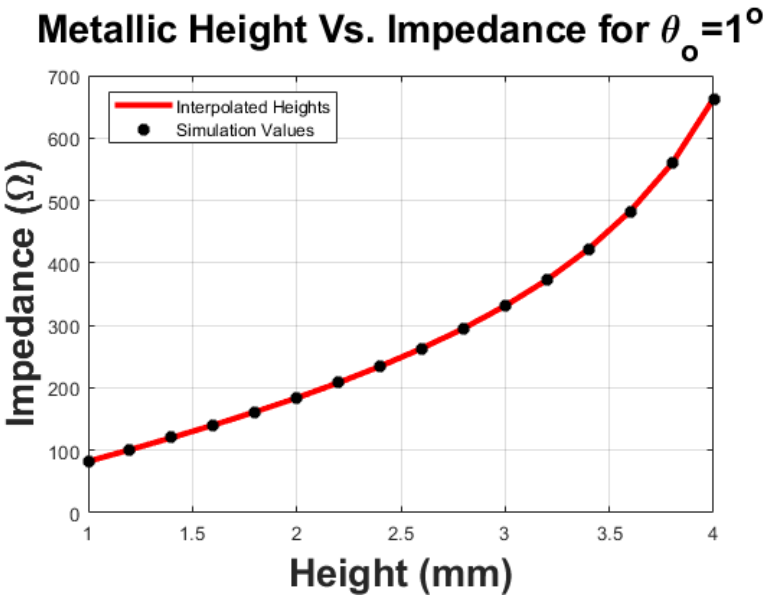

(a) Metallic Impedance-Height Database

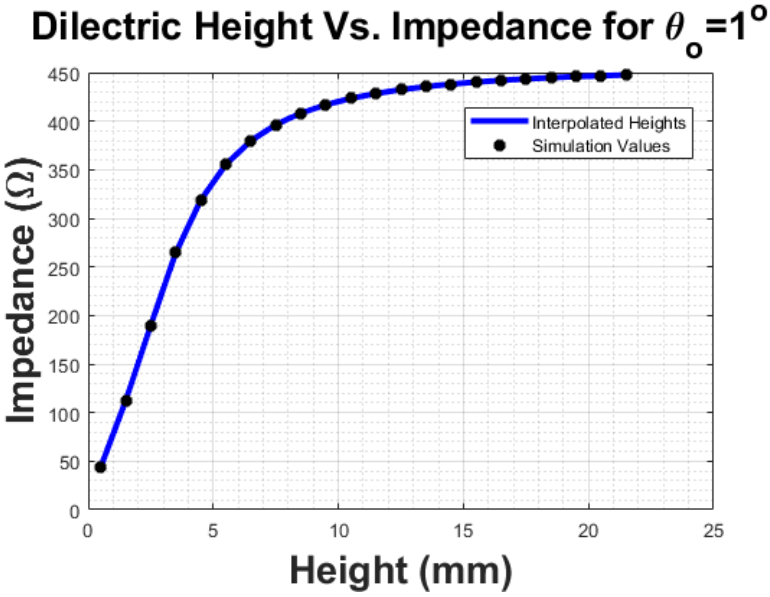

(b) Dielectric Impedance-Height Database

Figure 3.4: Database of impedance to corresponding height for the metallic and dielectric pins for a broadside design with the block dots calculated from simulation and the smooth colored line interpolating those values

index of $M = 0.65$ and $X_{av} = 0.7/\zeta$. The period is divided by N, which is six, and the impedance is taken at the center value of each section represented as black dots in Fig. 3.5. The black dots are the values of the individual pins for an impedance

considered at the center of the unit cell.

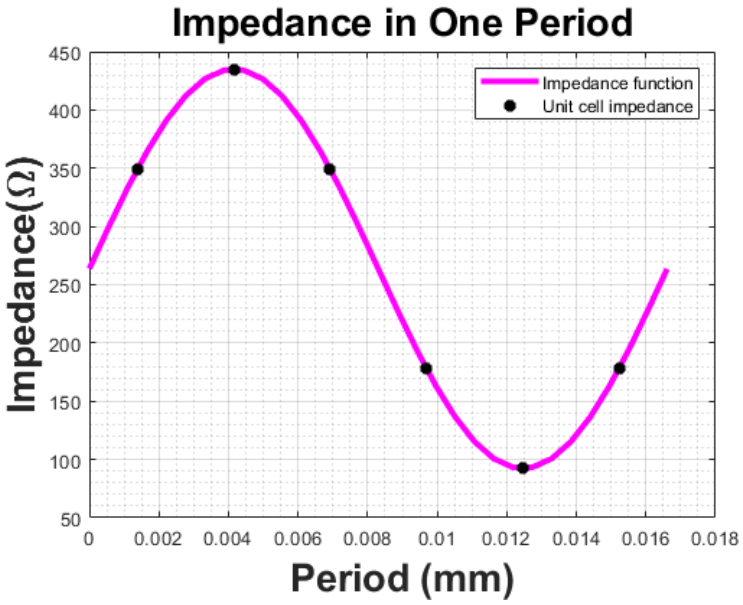

Figure 3.5: Impedance of one period for a one-dimensional modulation with the magenta line representing the modulation and the black dots representing the impedance of the individual unit cells for an impedance taken at the center of the cell

The values of the impedance and the corresponding metallic pin heights are shown in Table 3.1 for the metallic pins.

Table 3.1: 1D Modulation Impedance and Height for Metallic Broadside Antenna

Cell in Modulation	**Impedance (Ω)**	**Height (mm)**
1	349.42	3.09
2	435.12	3.45
3	349.42	3.09
4	178	1.95
5	92.3	1.11
6	178	1.95

The values in Table 3.1 are used to create a one-dimensional sinusoidally modulated metallic structure as shown in Fig. 3.6. The same process can also be applied to the dielectric pins, but only the metallic setup will be demonstrated for the one-dimensional case. Periodic boundaries are applied the front and back of the air box

and a radiation boundary is applied to the top. The dark blue boxes are perfect electric conductors (PEC) and are sized so the tops of the pins are aligned allowing the surface wave to "leak" as it travels across the pins. Theoretically, the pins should not need to be aligned on top, but the wave cannot penetrate the PEC. Aligning the tops of the pins helps increase the interaction of the surface wave by eliminating the ability of the wave to go in between the spaces of the pins. On the other hand, the wave can penetrate dielectric, so the the pins do not need to be aligned on the top to increase the interaction of the surface impedance and the surface wave.

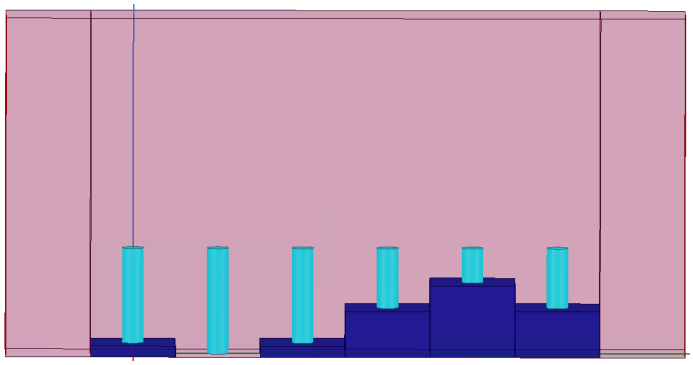

Figure 3.6: One period of modulation for a one-dimensional metallic broadside design

For the wave to fully radiate and display the leaky-wave behaviors, multiple periods need to be connected. Because this is the one-dimensional case, the periods contain the same six pins that repeat every period. Figure 3.7 shows six periods of modulation, equating to a length of 5λ, and the corresponding electric field when the structure is excited on the left port. The figure clearly shows the field strength dissipating as it crosses the length of the structure due to the field radiating upwards. With more periods, the field completely disappears by the time it reaches the opposite port. Another important note is the size of the air box for the periodic structure. Pictured, the air box has a height of five times the period. If the air box is too short, the field does not have the space to radiate and portray proper leaky-wave behaviors. Oppositely, if the air box is too tall, the wave begins to curve as it radiates upward

and creates side lobes in the electric field.

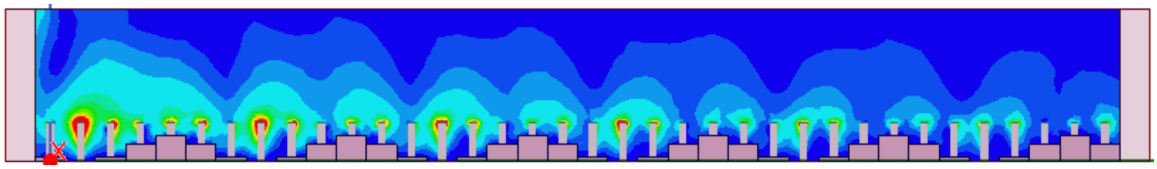

Figure 3.7: Six periods of modulation for a one-dimensional metallic broadside design electric field

Fig. 3.8 shows the directivity of the metallic periodic structure designed to operate with the pointing angle of $\theta_o = 1^o$ and the structure performing as designed. The figure clearly shows the main lobes pointing at 1^o when $\phi = 90^o$. The directivity is taken at this point to make sure the directivity shows the field as a cut of the antenna. There is a small side lobe in the directivity plot, but the magnitude is small enough that it can be ignored.

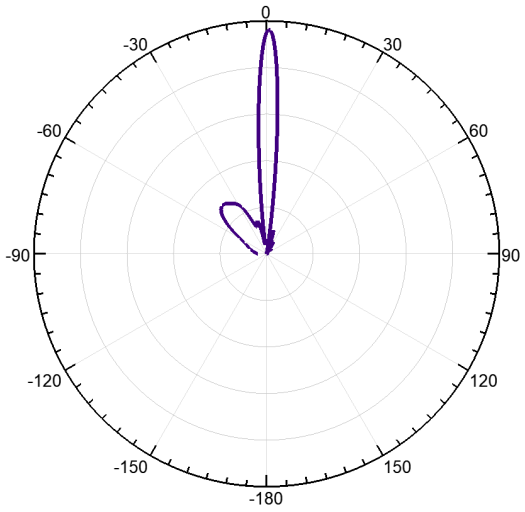

Figure 3.8: Polar plot of directivity for the metallic broadside antenna

3.2 Versatility of Pointing Angles

This section delves into three different design angles. The metallic antenna is designed for a pointing angle of $\theta_o = 10^o$. The dielectric antenna is designed for $\theta_o = 30^o$ and then rotated to demonstrate backward radiation.

3.2.1 Broadside Propagation

Section 3.1 covered the theory, math, and design for a one-dimensional modulation along the x axis. This section expands Eq. 3.2 to cylindrical coordinates with modulation dependent of both ρ and ϕ. The isotropic representation of the cylindrical sinusoidally modulated surface can be expressed as:

$$X_s(\rho, \phi) = X_{av}(1 + M \sin(\beta_{sw}\rho - k\rho \sin\theta_o \cos\phi \pm \phi)) \tag{3.7}$$

where $\rho = \sqrt{x^2 + y^2}$ and $\phi = \arctan(y/x)$. To allow the wave to fully radiate, the radius of the antenna is chosen to be 5λ which is equal to six periods, seeing as the wave was almost able to completely radiate over this length in the one-dimensional design. Due to the pointing angle being the same value as the design in section 3.1, the same database can be used for the two-dimensional antenna meaning the unit cell size, pin radius, and period of modulation are the same. Using the database created from the interpolated values in Fig. 3.4, a map of the pin heights is constructed for the design dependent on both ρ and ϕ by matching the correlating impedance to the respective pin height. Lastly, to ensure the map of the heights is accurate, an error plot is constructed by comparing the desired impedance value for each individual pin from Eq. 3.7 to what is available in the impedance height database in Fig. 3.4. Provided in Fig. 3.9 are the plots for the desired impedance, pin height, and error for a metallic pin antenna with a pointing angle of 1^o and an antenna radius of 5λ. The required impedance for this antenna design ranges from 92.3 Ω to 435 Ω which is covered using pin heights that range from 1.11 mm to 3.44 mm respectively. The impedance plot is shown with the impedance positions in respect to the x and y axis with each grid block indicating an individual pin impedance. Since there are six pins per period of modulation and six periods of modulation, the diameter of the antenna

consists of 72 pins. As clearly shown, although the individual pins have a single value of impedance, the overall impedance of the surface appears modulated.

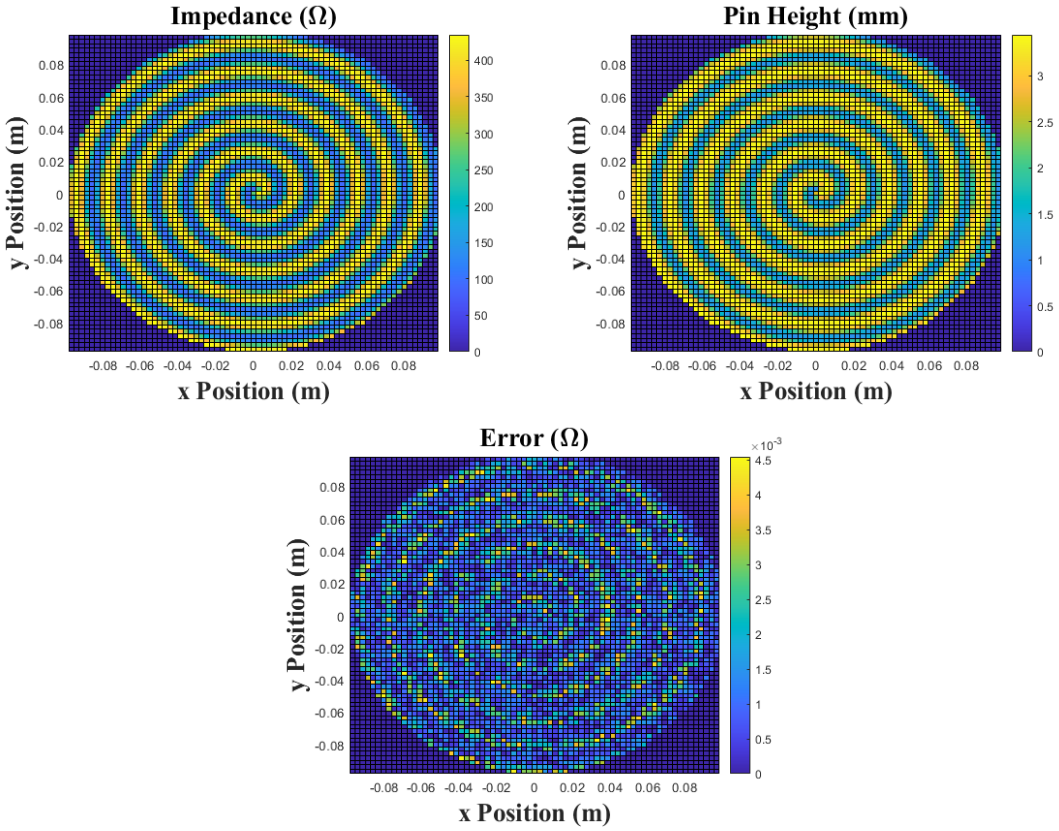

Figure 3.9: Impedance map, pin height map, and respective error map for metallic antenna designed for broadside propagation with a radius of 5 λ

The same impedance pattern is applied to a dielectric antenna with the same pointing angle of 1^o since material does not effect the impedance modulation. To achieve the impedance range of 92.3 Ω to 435 Ω, the dielectric pins vary from 1.21 mm to 13.38 mm. Since the wave does not radiate as quickly with the dielectric pins as it does with the metallic pins, the antenna radius is expanded to 9 λ to allow the wave to fully radiate across the surface. Recall the radius of the dielectric pins is 1.35 mm and the unit cell size if 2.77 mm.

Figure 3.10(a) shows the top view of the antenna showing the periodic unit cells with the pins in the center. Although the modulation of the heights cannot be seen

in this view, it nicely shows the periodicity of the surface. Figure 3.10(b) is the constructed antenna exemplifying the modulation. Again, the metallic pins are aligned on top and are sitting on varying size PEC boxes. For the dielectric antenna, the pins are simulated using acrylonitrile butadiene styrene (ABS) with a relative permitivity of $\epsilon_r = 3$ and not placed on any box to line the tops of the pins.

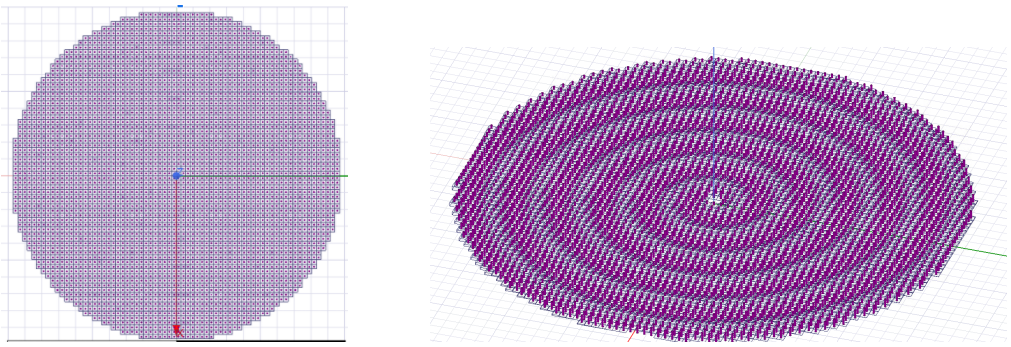

(a) Top view of antenna (b) Constructed antenna in HFSS

Figure 3.10: Metallic antenna for broadside propagation build

To simulate the structure using HFSS, the antenna is place on a PEC sheet. An air box with perfectly matched layer (PML) boundaries on all sides, except the bottom surface of the air box, is placed around the antenna ensuring the air box is at least $\lambda/4$ larger than the antenna at all points. The bottom surface of the air box has an additional PEC boundary assigned. A small circle of pins at the center of the antenna are removed. The extra space created by removing the pins allows the inserted small dipole excitation to have enough space to effectively radiate. The dipole inserted has a radius of 0.1 mm, a half dipole length of 1 mm, and a gap between the two half dipole cylinders of 0.1 mm. For all further antennas, this is the excitation method used other than the one specifically mentioned that is excited with a waveguide. The antenna is simulated at a frequency of 15 GHz and the electric field and directivity are recorded.

Figure 3.11 shows the results of the magnitude of electric field for the metallic antenna from a top view on a sheet placed approximately 1 mm higher than the

top of the pins. The concentration of the field is clearly the strongest at the dipole excitation. The pattern of the field is indicative of the upward radiation conveyed through the field weakening as the wave travels outward. The blue on the outside of the antenna proves the antenna is not radiating outside the antenna.

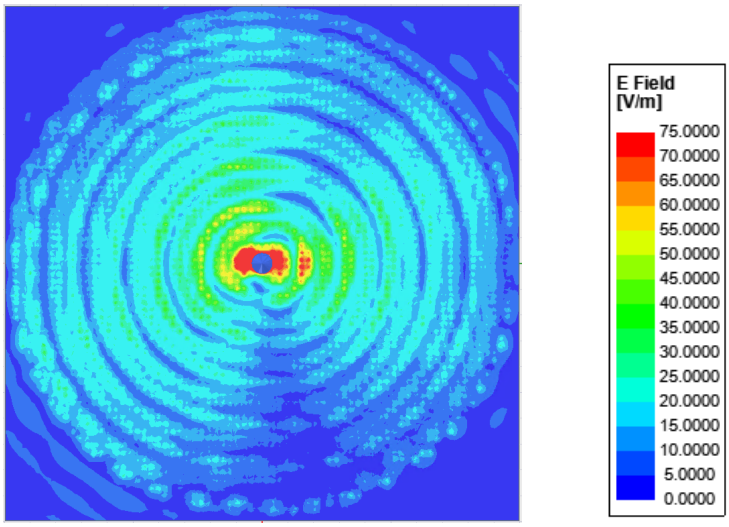

Figure 3.11: Electric field for metallic broadside antenna

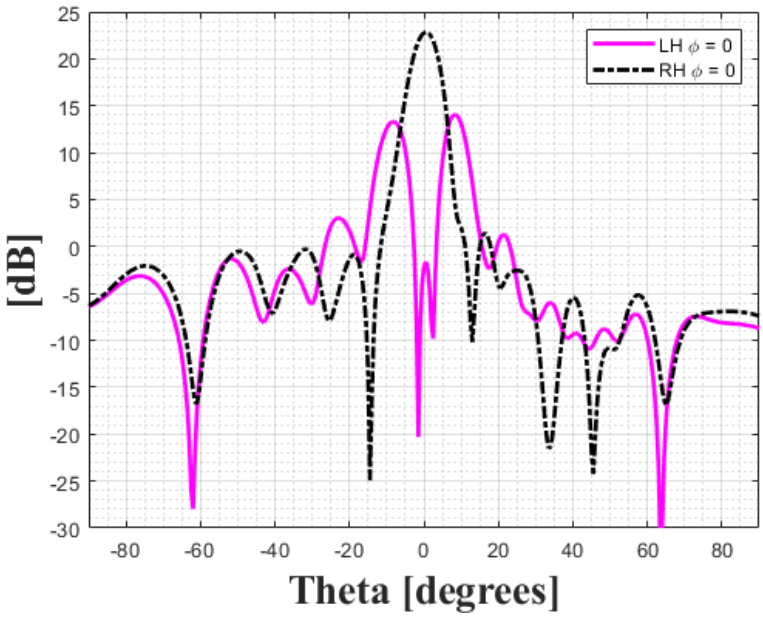

Figure 3.12: LHCP in magenta and RHCP in dashed black for metallic broadside antenna

Figure 3.12 and Fig 3.13 show the left hand circular polarization (LHCP) in magenta and the right hand circular polarization (RHCP) in black for $\phi = 0^o$ for the metallic and dielectric antenna respectively. The RHCP shows a peak at $\theta_o = 1^o$ proving the design method worked properly. The gain of the antenna at $\theta_o = 1^o$ for the metallic structure is approximately 24 dB and the gain for the dielectric antenna is approximately 26 dB. Due to the extra size of the dielectric antenna, the gain is a bit higher. Subsequently, the dielectric antenna has more side lobes as well. Other than the small difference due to size, the fully metallic and the fully dielectric antenna performed very similarly.

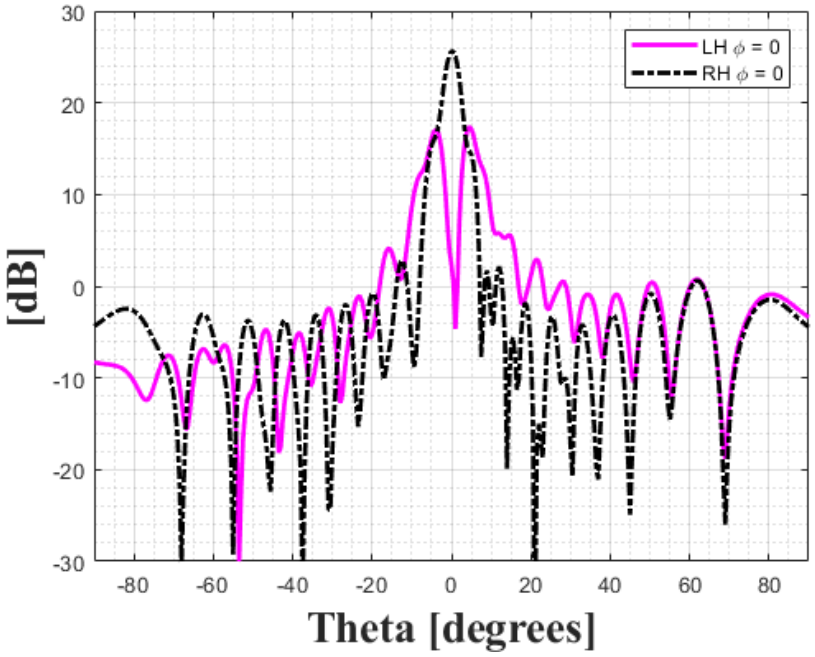

Figure 3.13: LHCP in magenta and RHCP in dashed black for dielectric broadside antenna

To test the bandwidth of the antenna, a circular waveguide is used to excite the dielectric antenna with a center frequency slightly higher than the antenna to guarantee the fundamental mode is excited. This antenna is operable in a broadband of frequencies as conveyed through the reflection coefficient, $S11$, in Fig. 3.14. S_{11}

crosses -10 dB at around 11 GHz, but stays consistently around -30 dB after 18 GHz. The broadband nature of this antenna allows it to be versatile in its functions.

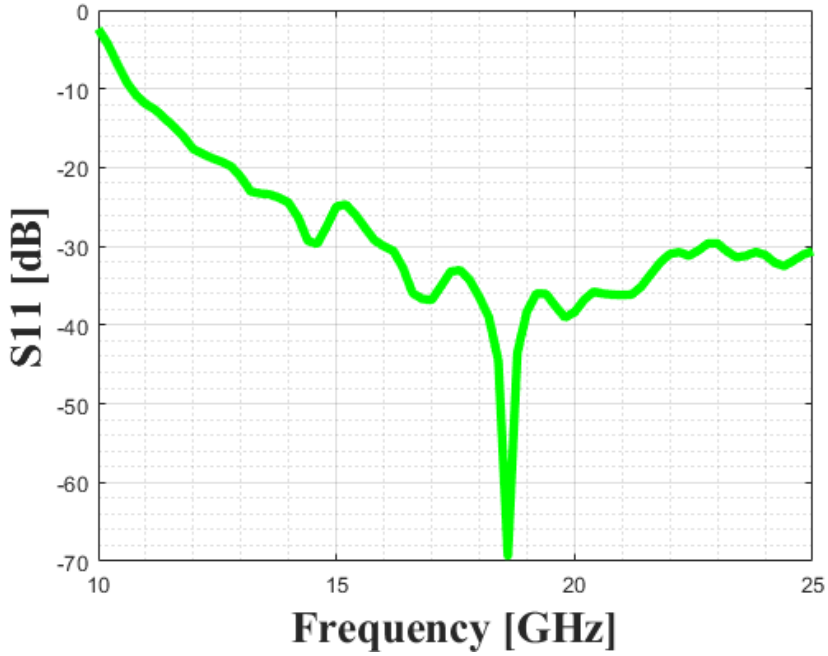

Figure 3.14: Bandwidth of broadside dielectric antenna

3.2.2 Angles Beyond Broadside

The antenna is designable for a large range of pointing angles including both positive and negative values. Three different angles and designs will be discussed and analyzed in this section. The metallic antenna example provided is designed to have a pointing angle of $\theta_o = 10^o$. Using Eq. 3.5, the period of modulation is 19.09 mm. With N=6, the unit cell size is 3.18 mm. The radius of the pin is also scaled up to adjust to the larger unit cell and becomes 0.403 mm. The radius of the antenna is kept the same from the broadside radiation design of 5λ. Although the value of θ_o changes, the range of impedance that is required to be covered using Eq. 3.7 is only negligibly effected. The lowest impedance for $\theta_o = 10^o$ is 92.3 Ω achieved with a pin height of 1.24 mm and the highest impedance is 435 Ω achieved with a pin height of

3.53 mm. The corresponding impedance map and respective pin height map is shown in Fig. 3.15 for a metallic antenna with a pointing angle of 10^o and antenna radius of 5λ. Notice the map for this angle is slightly asymmetric because it is not broadside.

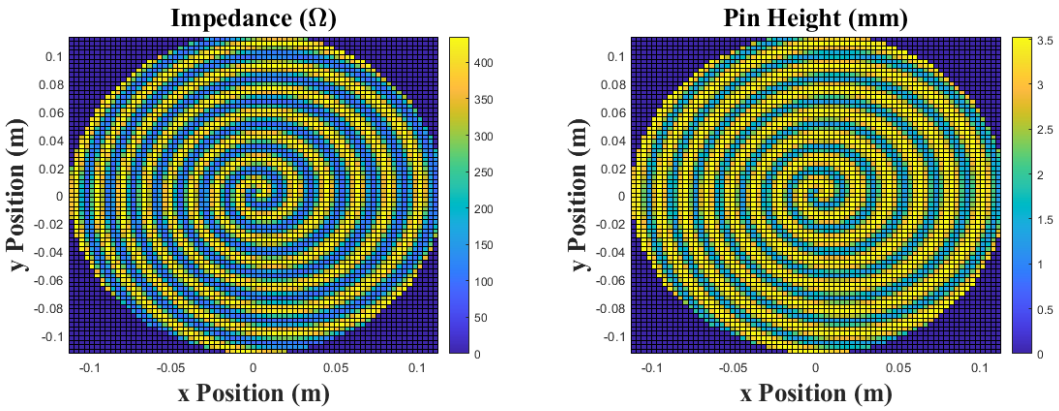

Figure 3.15: Impedance map and pin height map for metallic antenna designed for $\theta_o = 10^o$ propagation with a radius of 5 λ

The magnitude of the electric field for the non-broadside metallic antenna is shown in Fig. 3.16. The radiation is clearly the most concentrated at the dipole excitation and dissipates laterally across the antenna as it radiates upwards. The blue corners are indicative the antenna is not radiating outward because the field magnitude is zero by the time it reaches the edge of the antenna.

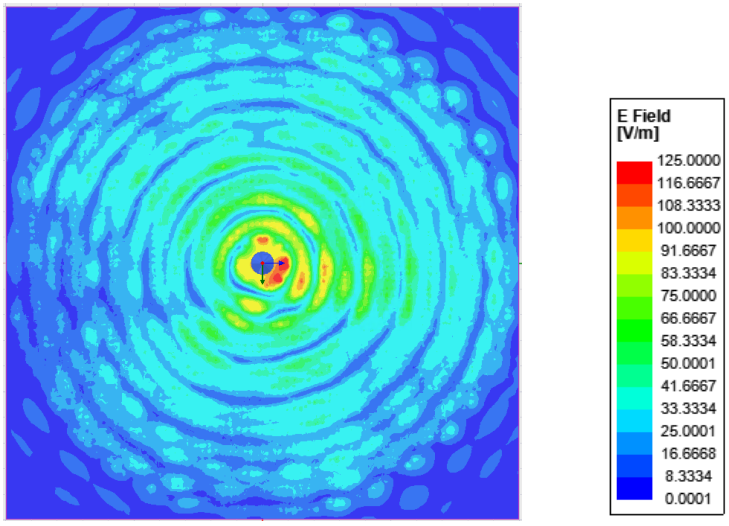

Figure 3.16: Electric field for metallic antenna designed for $\theta_o = 10^o$

Comparing Fig. 3.12 and Fig. 3.17, the results are almost identical other than the shift in the peak gain from $\theta_o = 1^o$ to $\theta_o = 10^o$. The gain of the RHCP is approximately 24 dB and the LHCP, the cross polarization, drops to below 0 dB.

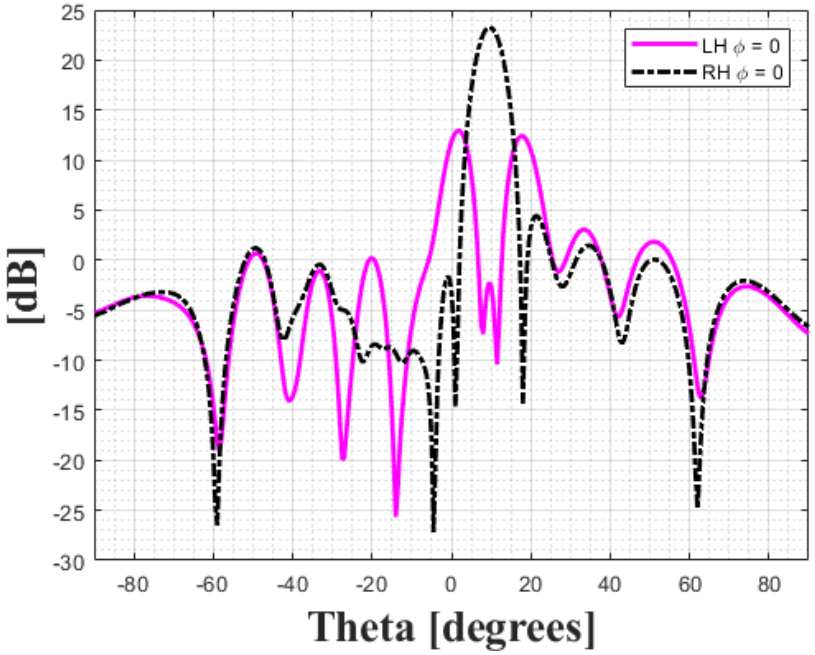

Figure 3.17: LHCP in magenta and RHCP in dashed black for metallic antenna designed for $\theta_o = 10^o$

For the purpose of showing the diversity of the antenna, the dielectric antenna is designed for a pointing angle of $\theta_o = 30^o$. Using Eq. 3.5, the period of modulation is 27.73 mm. With N=6, the unit cell size is 4.62 mm. The radius of the pin is adjusted to the larger value of 2.2 mm to accommodate the larger unit cell size. This dielectric antenna is designed to have a radius of 9λ to allow the wave to radiate to the edge of the antenna. The lowest pin height for this design is 1.19 mm for an impedance of 92.3 Ω and the tallest is 19.74 mm for an impedance of 435 Ω. Figure 3.18 shows the impedance, pin heights, and error of the data for the $\theta_o = 30^o$ dielectric antenna. The asymmetry for this design is a lot more apparent than $\theta_o = 10^o$ since it is far away from broadside propagation.

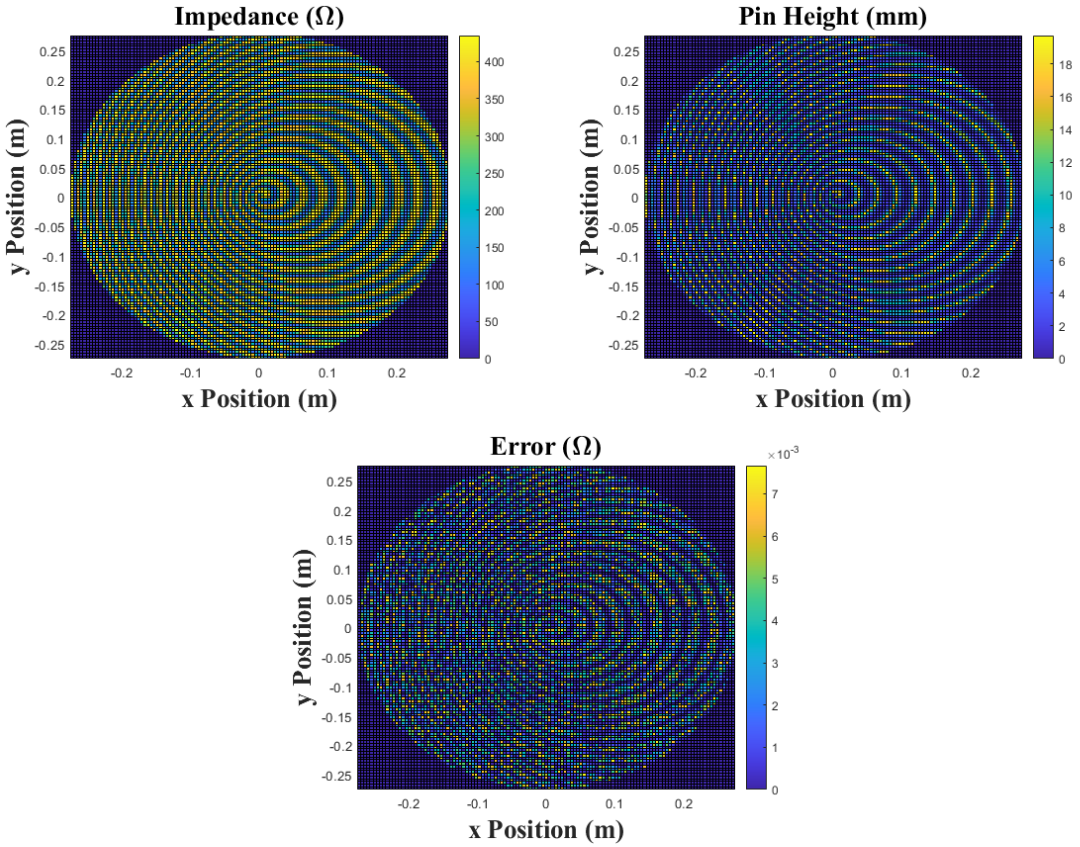

Figure 3.18: Impedance map, pin height map, and respective error map for dielectric antenna designed for $\theta_o = 30^o$ with a radius of 9 λ

The simulated dielectric antenna is shown in Fig. 3.19. The sinusoidal modulation becomes apparent with this type of antenna design.

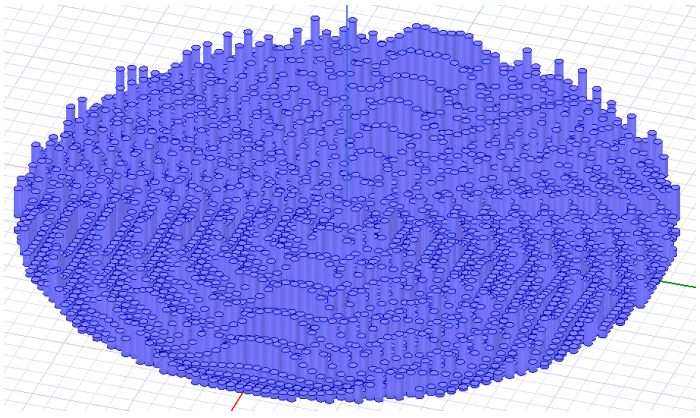

Figure 3.19: Constructed dielectric antenna designed for $\theta_o = 30^o$ with a radius of 9 λ in HFSS

To achieve a pointing angle of $\theta_o = -30^o$, the entire structure is rotated 180^o resulting in an impedance diagram shown in Fig. 3.20. This was accomplishments by subtracting 180^oc from the phase of each pin in order to rotate the structure.

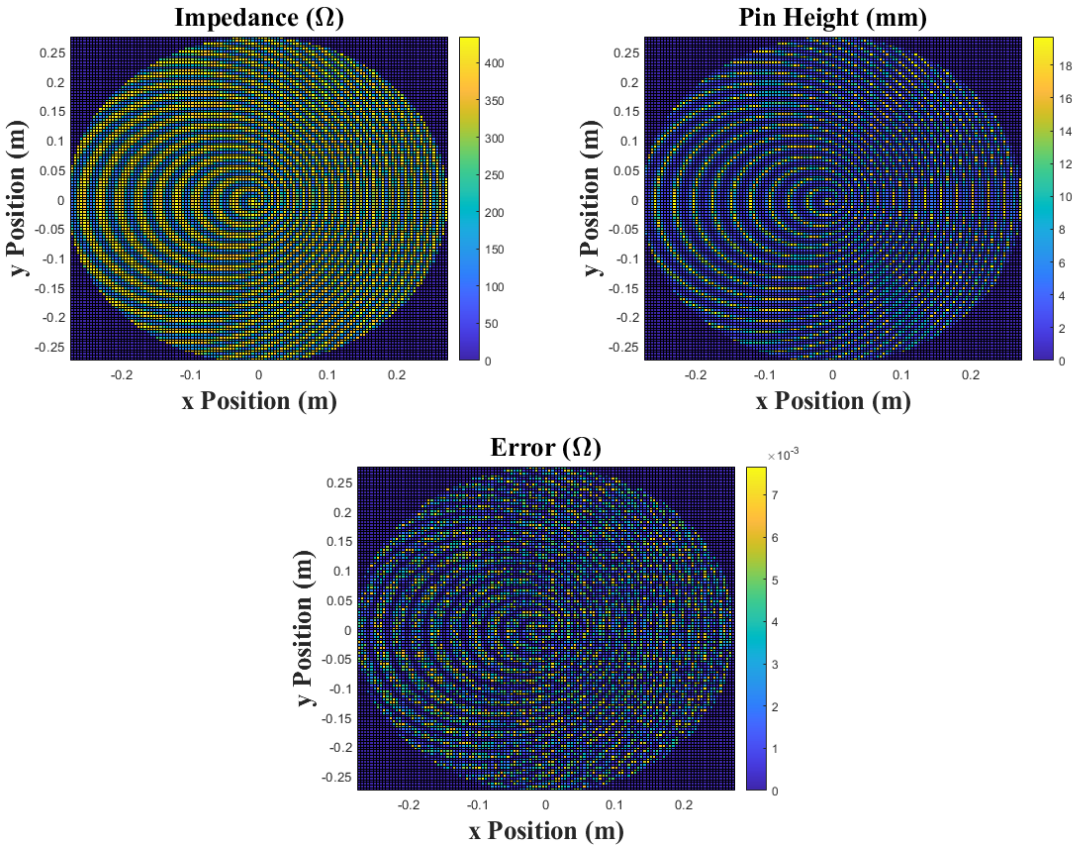

Figure 3.20: Impedance map, pin height map, and respective error map for dielectric antenna designed for $\theta_o = -30^o$ with a radius of 9 λ

The directivity of both positive and negative 30^o are shown in Fig. 3.21 and Fig. 3.22. The result of the $\theta_o = 30^o$ is similar to the previous data with the gain peak of the RHCP at the designed pointing angle and the cross polarization plummeting at that angle. The side lobes are all also relatively low in respect to the peak that occurs at approximately 22 dB. By rotating the antenna 180^o around the z axis, the antenna exhibits some interesting behavior. The peak gain of the RHCP occurs at the desired angle of -30^o with a value of 30 dB and the cross polarization plummets downward at that point. In addition, the side lobes become more extreme in respect

to the peak gain value.

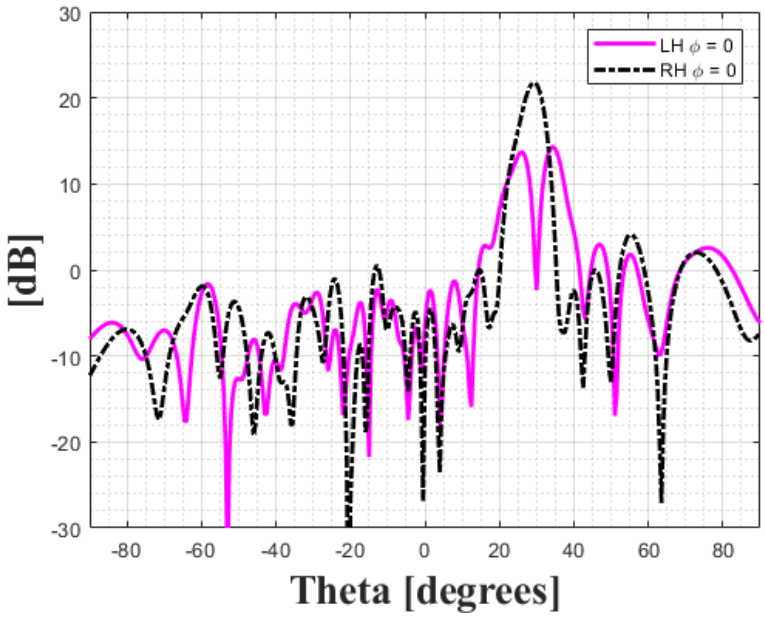

Figure 3.21: LHCP in magenta and RHCP in dashed black for dielectric antenna designed for $\theta_o = 30^o$

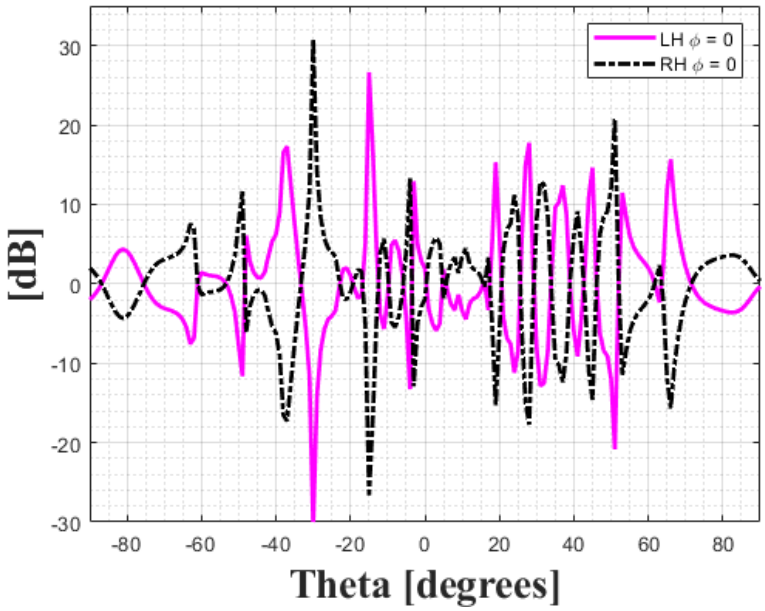

Figure 3.22: LHCP in magenta and RHCP in dashed black for dielectric antenna designed for $\theta_o = -30^o$

3.2.3 Fabrication

The frequency of operation was chosen for both antennas to be 15 GHz so the size of the antenna is additive manufacturable. This means the wavelength is approximately 20 mm and unit cells that are much much smaller than 20 mm are printable using a commercial 3D printer. The 3D printer the antennas will be printed with is the Raise3D Pro2 which can print with a layer height of 0.1 mm and accuracy of 0.005 mm. The printer is also capable of various type of filaments such as conductive or a typical plastic filament. The conductive filament that will be used to print the metallic antenna is Multi3D's Electrifi conductive filament that has a resistivity of 0.006 Ω cm. ABS will be used as the dielectric for additive manufacturing. ABS is a cheap, lightweight, and durable material making the fabrication of the dielectric antenna desirable. In addition, since the antenna is easy to design and cheap and quick to make, it is fast to go through the process of designing and creating for various applications.

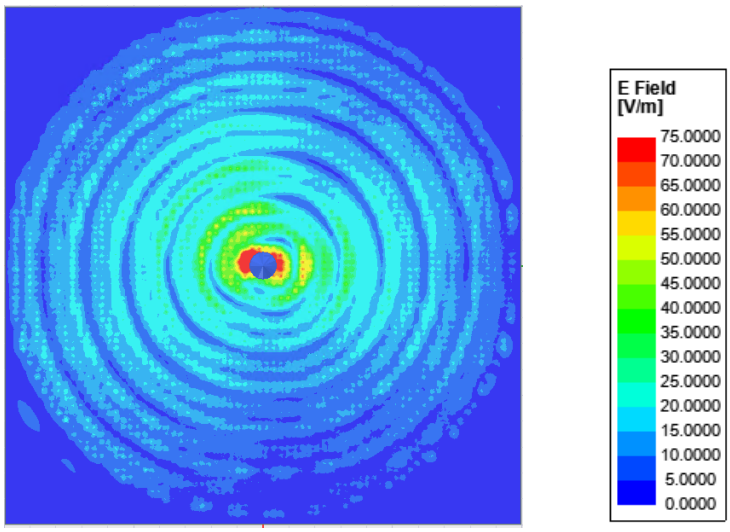

Figure 3.23: Electric field for metallic broadside antenna using conductive filament

The metallic antennas in the previous sections are simulated using a perfect electric conductor (PEC), but the metallic filament that can be used to create this has a bulk

conductivity of 16667 S/m. The antenna is resimulated for the $\theta_0 = 1^o$ design using this information and the electric field is plotted in Fig. 3.23 with the same scaling as the electric field from Fig. 3.11. The results using the PEC versus the conductive filament are nearly identical. The leaky wave behavior of the wave is not very effected as long as the conductivity of the material is high.

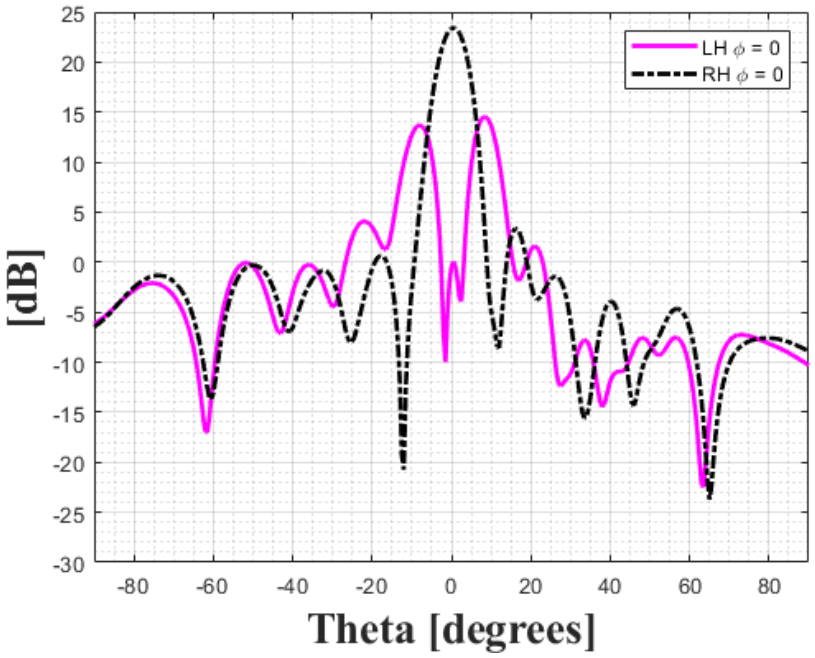

Figure 3.24: LHCP in magenta and RHCP in dashed black for metallic broadside antenna using conductive filament

The directivity of the $\theta_0 = 1^o$ metallic antenna using conductive filament is shown in Fig. 3.24. Again, the directivity is not effected by using a non perfect conductive material and has approximately the same gain and points in the same direction as the antenna designed with a PEC.

CHAPTER 4: POLARIZATION SPLITTING METASURFACE

Three-dimensional metamaterials that have an electrically large wavelength in respect to the unit cell are considered to be in the quasi-static region. Classical mixing formulas such as Maxwell's equations and Rayleigh scattering can be utilized to be able to find the electromagnetic properties of the material such as permitivity, ϵ ,and permeability, μ. The second region of operation is when the wavelength is relative to the size of or smaller than the unit cell such that the wavelength does not see the material as an effective medium. The metamaterials in this region are designed through a full-wave approach, but do not act as an effective medium. The last region occurs when the wavelength is large compared to the unit cell, but the unit cells can resonate which allows interesting behavior such as double negative materials. The material is considered a metamaterial at frequencies at which the unit cells resonate. In addition, the material is dispersive, but can be described with its electromagnetic properties because it acts as an effective medium [52].

These regions apply for both three-dimensional and two-dimensional materials. With a two-dimensional material that falls into the region with resonances, it is called a metasurface. These materials are typically created to operate in the fundamental mode due to the complexity of higher order Floquet-Bloch modes. There are a few types of metasurfaces dependent of their geometry. A metasurface that is created with apertures as the unit cell resembling a fishnet-like structure is considered a metascreen. Oppositely, a metasurface designed with isolated conductive patches as the unit cell is considered a metafilm. A metasurface with a combinations of both apertures and patches that does not have a specific name is considered a metasurface [52].

This chapter discuss a three layer polarization splitting metasurface composed of three layers of metallic patches in a dielectric slab. The first section will describe the theoretical design principles needed to be able to create this metasurface. The second section will detail the design approach to create the metasurface.

4.1 Design Principles

The concept of the metascreen is based on a generalization of Snell's Law provided in Eq. 4.1 due to the additional gradient of the phase represented by change of phase in respect to space divided by the wave number. The generalization of Snell's law states that the permitivity and phase of the first medium with an additional phase is related to the permitivity and phase of the second medium.

$$\sqrt{\epsilon_{r1}}\sin\theta_1 + \frac{1}{k}\frac{\delta\phi}{\delta x} = \sqrt{\epsilon_{r2}}\sin\theta_2 \tag{4.1}$$

The metascreen presented is derived of three layers of metallic period unit cells in a dielectric slab. The three layer approach to the metascreen design provides multiple degrees of freedom that can achieve perfect transmission and a large phase coverage [53,54]. For each polarization, a local transmission model representation can be utilized with each layer in the screen represented by a shunt admittance as shown in Fig. 4.1 where k_z is the wave number of free space above and below the screen with a corresponding impedance of Z_0 for the excited mode. Also, in reference to the figure, k_{z1} is the wave number of the dielectric slab of the screen with a corresponding impedance of Z_1 for the excited mode.

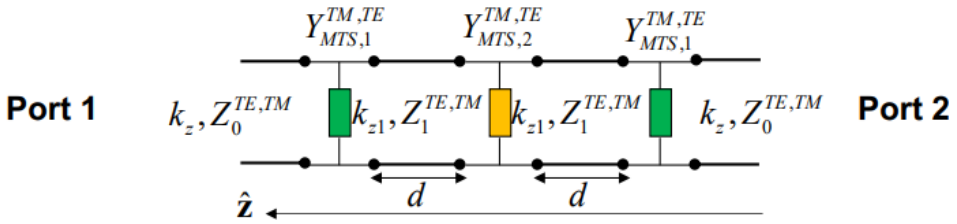

Figure 4.1: Local transmission line model for metascreen for single polarization

The wave number, k_z, is denoted by $k_z = k_0\sqrt{1-\sin^2\theta_i}$ where θ_i is the incident wave; if the incident wave is 0^o, k_z is equal to k_0. The wave number of the dielectric is defined as $k_{z1} = k_0\sqrt{\epsilon_r - \sin^2\theta_i}$ where ϵ_r is the relative permitivity. The impedance of free space for a transverse magnetic excited wave is related as $Z_0^{TM} = \frac{\zeta_0 k_z}{k_0}$ and simplified to just the free space impedance when the incident angle is 0^o. The impedance of a free space transverse electric wave is $Z_0^{TE} = \frac{\zeta_0 k_0}{k_z}$ and simplified to free space impedance with an incident angle of 0^o. Similarly, the impedance of the dielectric for a TM wave is $Z_1^{TM} = \frac{\zeta_1 k_{z1}}{k_1}$ and is $Z_1^{TE} = \frac{\zeta_1 k_1}{k_{z1}}$ for a TE wave.

Fig. 4.1 can be solved using the the transmission matrix which is referred to as the $ABCD$ matrix. The $ABCD$ matrix utilized for this local transmission line model is a two-port network. The $ABCD$ matrix is defined as:

$$\begin{bmatrix} V_1 \\ I_1 \end{bmatrix} = \begin{bmatrix} A & B \\ C & D \end{bmatrix} \begin{bmatrix} V_2 \\ I_2 \end{bmatrix} \tag{4.2}$$

where the $ABCD$ matrix is the admittance matrix of the two port network [55]. For the metascreen and the transmission representation in Fig. 4.1, the $ABCD$ matrix for the dielectric slab is expressed as:

$$ABCD_d = \begin{bmatrix} \cos(k_{z1}d) & jZ_1^{TM,TE}\sin(k_{z1}d) \\ j\frac{1}{Z_1^{TM,TE}}\sin(k_{z1}d) & \cos(k_{z1}d) \end{bmatrix} \tag{4.3}$$

Since the transmission line is represented as a shunt admittance, the individual values of the metascreen layers are seen as the C position in the matrix. The $ABCD$ matrices for the two different screen admittances can be defined as:

$$ABCD_{MTS,1} = \begin{bmatrix} 1 & 0 \\ Y_1^{TM,TE} & 1 \end{bmatrix} \tag{4.4}$$

$$ABCD_{MTS,2} = \begin{bmatrix} 1 & 0 \\ Y_2^{TM,TE} & 1 \end{bmatrix} \tag{4.5}$$

The total admittance of the screen can be solved by multiplying the $ABCD$ matrix of each section of the transmission line starting from the left with the first screen layer and passing through the dielectric, the second layer of the screen, another dielectric, and finally the last screen layer. This is shown by:

$$ABCD_{tot} = ABCD_{MTS,1}ABCD_dABCD_{MTS,2}ABCD_dABCD_{MTS,1} \tag{4.6}$$

Using the $ABCD_{tot}$ matrix, the reflection coefficient and the transmission coefficient can be expressed in Eq. 4.7 and Eq. 4.8 written in a generic form to include both TM and TE excitations.

$$S_{11} = \frac{A + B/Z_0^{TM,TE} - CZ_0^{TM,TE} - D}{A + B/Z_0^{TM,TE} + CZ_0^{TM,TE} + D} \tag{4.7}$$

$$S_{21} = \frac{2(AD - BC)}{A + B/Z_0^{TM,TE} + CZ_0^{TM,TE} + D} \tag{4.8}$$

The transmission line is thus solved to achieve the reflection coefficient, S_{11}, equal to zero and transmission coefficient, S_{12}, equal to $e^{j\phi}$ where ϕ is the phase shift in the polarization. Equation 4.9 shows the representation of the impedance of the outer screens and Eq. 4.10 is the impedance of the middle screen to achieve the desired

scattering parameters.

$$Y_1 = \frac{j}{Z_d \tan(k_d d)} + \frac{j}{Z_0 \tan\left(\frac{\phi}{2}\right)} \tag{4.9}$$

$$Y_2 = \frac{j\left[Z_0 \sin\left(\frac{\phi}{2}\right) + Z_0 \sin\left(\frac{3\phi}{2}\right) + 2Z_d \sin(2k_d d)\cos\left(\frac{\phi}{2}\right)\right]}{2Z_d^2 \cos\left(\frac{\phi}{2}\right)\sin^2(k_d d)} \tag{4.10}$$

Due to the dual polarization of the presented metascreen, the impedances can be represented as tensors as shown in Eq. 4.11 and Eq. 4.12. This representation shows that the impedance is dependent on whether the propagating wave is in the x direction or in the y direction thus producing different deflected angles dependent on the polarization.

$$Y_1 \rightarrow= \underline{\underline{Y}}_1 \begin{bmatrix} Y_1^{xx} & 0 \\ 0 & Y_1^{yy} \end{bmatrix} \tag{4.11}$$

$$Y_2 \rightarrow= \underline{\underline{Y}}_2 \begin{bmatrix} Y_2^{xx} & 0 \\ 0 & Y_2^{yy} \end{bmatrix} \tag{4.12}$$

The screen between air and dielectric is locally modeled in Fig. 4.2 with the left half of figure as a snippet of the transmission line model and right half shows the wave propagating into the screen and dielectric and the reflection in air.

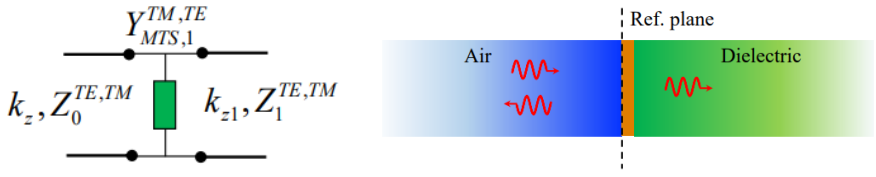

(a) Transmission line model (b) Pictorial representation

Figure 4.2: Local model of Y_1 impedance

The impedance of metascreen, Z, can solved using the reflection coefficient as shown in Eq. 4.13.

$$Z_{Y1} = Z_0^{TM,TE}\frac{1+S_{11}}{1-S_{11}} \tag{4.13}$$

Equation 4.13 can be substituted into Eq. 4.14 where $Y_1^{TM,TE}$ is $1/Z_1^{TM,TE}$ in order to obtain the admittance of the outer layers of the metasurface.

$$Y_{MTS,1}^{TM,TE} = \frac{1}{Z_{Y1}} - Y_1^{TM,TE} \tag{4.14}$$

The same process is used to determine the admittance of the middle layer of the middle screen, but the two surrounding materials are dielectric. The impedance of the middle layer is:

$$Z_{Y2} = Z_1^{TM,TE}\frac{1+S_{11}}{1-S_{11}} \tag{4.15}$$

Equation 4.15 is substituted into Eq. 4.16 to obtain the impedance of the middle layer of the metascreen.

$$Y_{MTS,2}^{TM,TE} = \frac{1}{Z_{Y2}} - Y_1^{TM,TE} \tag{4.16}$$

4.2 Design Approach

The electric field used to excite the metasurface is a plane wave which is defined as $E_y = E_0 e^{-jkz_p}$. Considering the plane wave is excited in free space, the magnetic field can be expressed through dividing the electric field by the free space impedance,

or $H_y = \frac{-E_y}{\zeta}$. The phase of the screen can be obtained by adding the phase of the incoming field and incorporating the holographic principle. The holographic principle in microwave applications utilizes a source wave as a reference to another wave interference to create an image of the resulting radiation pattern. Equation 4.17 shows the phase of the screen with the phase of the initial field subtracted with the holographic principle.

$$\Phi_{screen} = -\angle E_y - k\sin(\theta_0 Y) \tag{4.17}$$

When exciting with a plane wave, the phase is considered constant and can be assumed to be zero since there are no interferences making Eq. 4.17 equal to $-k\sin(\theta_0 Y)$. The phase of the three-layer screen becomes the phase of the transmission coefficient since the the excitation wave is a plane wave. Figure 4.3 shows the magenta, thicker line as the phase of the screen using Eq. 4.17 and the blue, thinner line shows the transmission phase using the $ABCD$ matrix method. This graph proves mathematical the screen should perform as predicted.

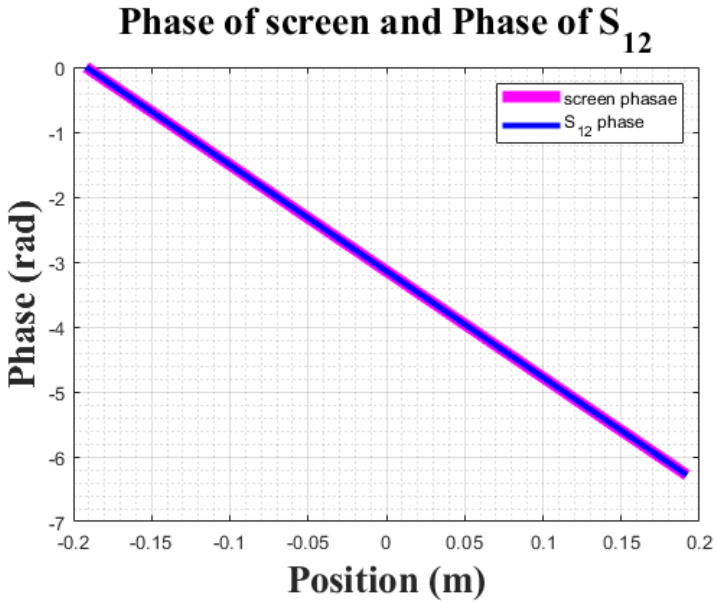

Figure 4.3: Phase of the screen plotted against phase of transmission coefficient

To prove the beam shifting using a surface impedance to create a phase variance is feasible, a surface impedance to create a beam steering of 10^o was designed. The required impedance values for the surface for the varying positions were imported into Comsol to create a two-dimensional simulation. In the center of Fig. 4.4, the darker black line is the placement of the screen with the two dielectric layers in the middle. The height of the dielectric layers for this simulation are both $\lambda/250$. The top and bottom layers are assigned an impedance map that correlates to Y_1 and the middle layer has an impedance equivalent to the calculated Y_2. Figure 4.4 clearly shows the plane wave steering 10^o with normal incidence once it passes through the screen indicating the desired behavior is accomplished.

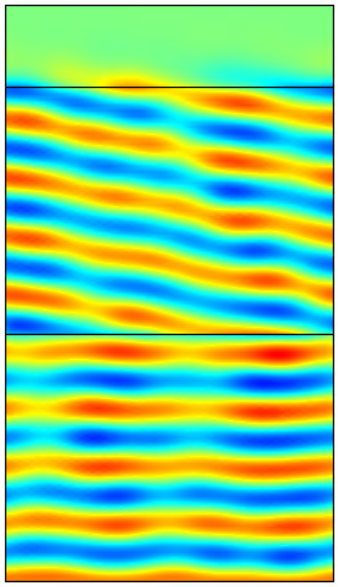

Figure 4.4: Simulation of normal incidence with the beam steered 10^o

Figure 4.4 shows a singularly polarized screen, but the screen proposed is dually polarized and performs as a polarization splitter. This means that depending on whether the screen is excited with a TE wave or TM wave, the resulting wave is deflected to a different angle since the incident wave sees difference impedance values. The new local model to represent this screen is shown in Fig. 4.5 with the black electric and

magnetic field corresponding to a TM polarization and the red electric and magnetic field corresponding to a TE polarization with their respectively reflected waves when the distance between the screen are much much smaller than the wavelength.

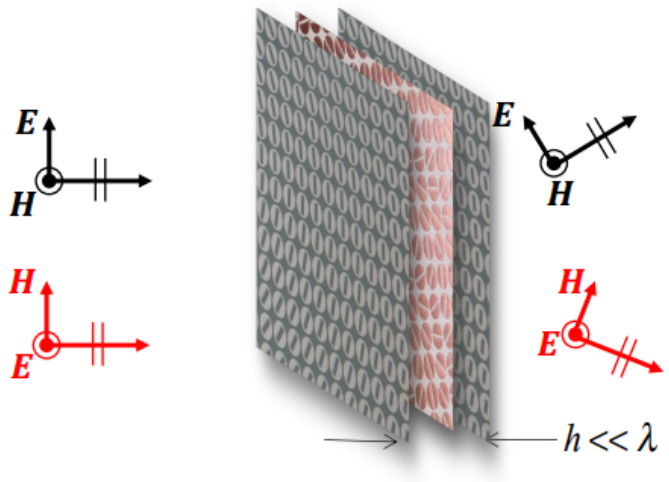

Figure 4.5: Dual polarization model showing electric and magnetic field for each polarization

The distance between the screens makes a large impact on the results of the metasurface behavior. The distance between the layers of the screen has to be small enough to prevent phase shifts from the higher order Floquet modes that compound from screen to screen introducing complexity into the design that would prevent it from working. If the layers of the screen are too close, the wave will see the screen as one block of impedance instead of three individual layers of screens preventing the screen from working. The distance between the layers for the proposed metasurface is 0.5 mm.

Using an example of unit cell to create the screen, the independent polarizations are shown in Fig. 4.6. The left figure is a x-polarized wave excited with a TM mode wave and the right figure shows an y-polarized wave excited with a TE mode wave. Due to the dual polarization, the transmission line model representing the metasurface has

to be reconsidered to account for the polarization in both the x and y direction as shown in Fig. 4.7. The difference between this transmission line model and Fig. 4.1 is that the impedances are now dependent on their polarization.

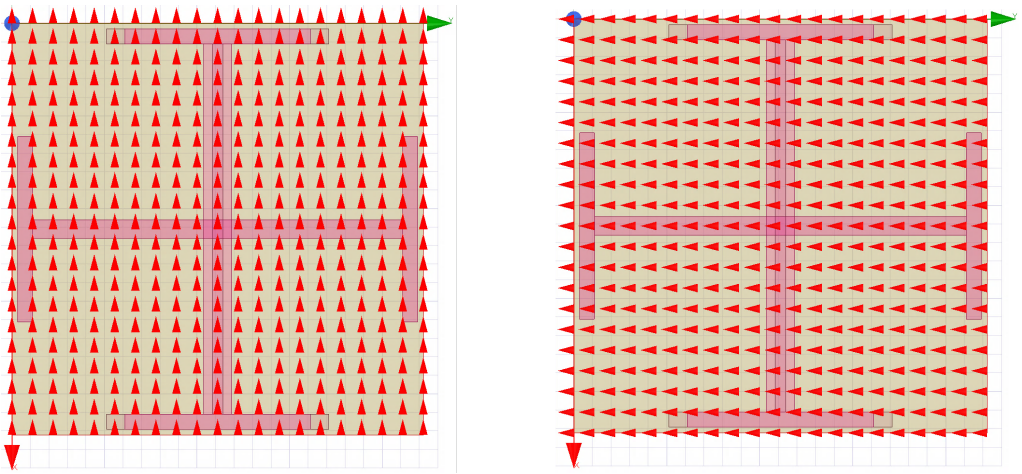

(a) X-Polarization (b) Y-Polarization

Figure 4.6: Two different mode excitations on an example unit cell showing the independent polarizations

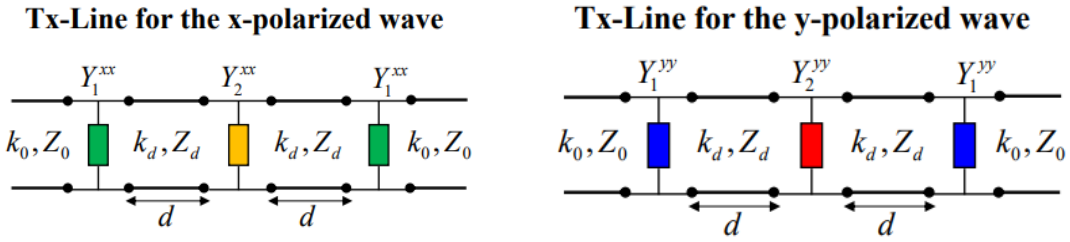

(a) X-Polarization (b) Y-Polarization

Figure 4.7: Local transmission line model for metasurface for single polarization

To obtain the phase coverage needed to create the metasurface, the screen is designed with five different unit cells. The unit cells produce phases that are approximately 72^o apart starting at 36^o. Due to adjacent unit cells being different, an infinite periodicity assumption is not completely accurate. As the capacitance between cells increases, the inaccuracy of the model also increases. Because the metasurface can be described using transmission line theory, the increased capacitance also means

increased bandwidth. There is a direct trade-off between the bandwidth and the accuracy of the local periodicity assumption. By using five unit cells equally spaced, the local periodicity assumption can still be accurately used and a large bandwidth can also be accomplished [53].

4.3 Optimization of Design

The design of the metasurface uses five different unit cells to create the modulation phase to create the beam steering angle. The basic design of all the unit cells are inspired by a Jerusalem cross. Figure 4.8 shows the basic shape and the changing parameters for the middle layer of the metasurface. The top and bottom layer also are derived using this shape, but the name of parameters are in term of b instead of a. For example, $a1$ becomes $b1$ and and w_la1 is w_lb1. All the variables that change the shape changing the impedance for x polarization end with a 1. Not labeled, but the other excitation would be changed with variables labeled 2 to ensure the shape is not symmetric and can act with independent polarization.

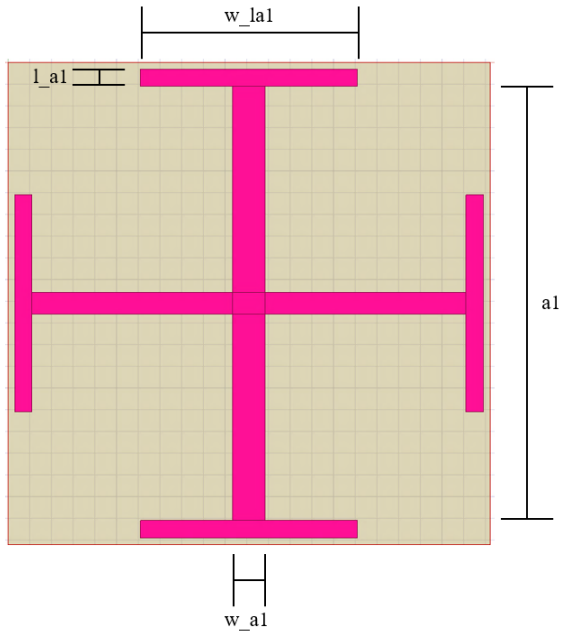

Figure 4.8: Basis of unit cell design with parameters labeled

Using the pattern search optimization option in HFSS, the individual unit cells were varied for both the top and bottom layer and the middle layer to find the five different phases that span -180^o to 180^o. Table 4.1 shows the values of the parameters for their respective phase. For 36^o and 108^o, the basic cross shape was not able to be varied in a way to accomplish these phases. To create the higher phase of 108^o, a capacitive element was added to both. To achieve a phase with a magnitude of at least half power, a capacitor-like shape with plates having a thickness of 0.25 mm and distanced by 0.5 mm is added to the middle layer. Using an optimization search in HFSS, the best position was found such that the start of the capacitor shape is shifted 4 mm from the top and bottom flanges. The positioning of this creates a square in the middle of the unit cell which raises the magnitude of the opposite polarization a small amount, but the magnitude of the opposing polarization remains under 0.1. To introduce more inductance into the unit cell to create a phase of 36^o, two smaller rails are added adjacent to either side of the middle rail of the unit cell. The extra rails are offset from the center rail by 0.5 mm and have the same height as $a1$ with a width of 0.2 mm. In addition, a small hole is cut from the top and bottom flanges introducing capacitive behavior from the gap and inductive behavior from the loop formed. The hole is a ratio of the two-dimensions that define that flange with the horizontal component of $w\_la1/2.4$ and the vertical component with a cutout size of $l\_a1/2$. Again, the hole dimensions along with the placement and size of the additional rails are found using the pattern search optimization method in HFSS.

Table 4.1: Unit Cell Parameter Specifications Per Phase

ϕ	w_a1	w_b1	w_la1	w_lb1	l_a1	l_b1
36^o	0.5 mm	0.5 mm	8 mm	7 mm	0.481 mm	0.4 mm
108^o	0.5 mm	0.51875 mm	4.35 mm	7 mm	0.481 mm	0.4 mm
-180^o	2.5 mm	1 mm	6 mm	7 mm	0.5 mm	0.5 mm
-108^o	0.5 mm	0.456 mm	7.3 mm	4.88 mm	0.4 mm	0.5 mm
-36^o	0.275 mm	0.75 mm	6 mm	7 mm	0.5 mm	0.5 mm

The individual unit cells for each phase for the top and bottom layer, Y_1, are shown in Fig. 4.9 and their respective middle layer, Y_2, shown in Fig. 4.10. The left and right flanges are 5 mm as to prevent any coupling between the side flanges and the top flanges. This ensures the modes will not be effected by the opposite polarization parameters.

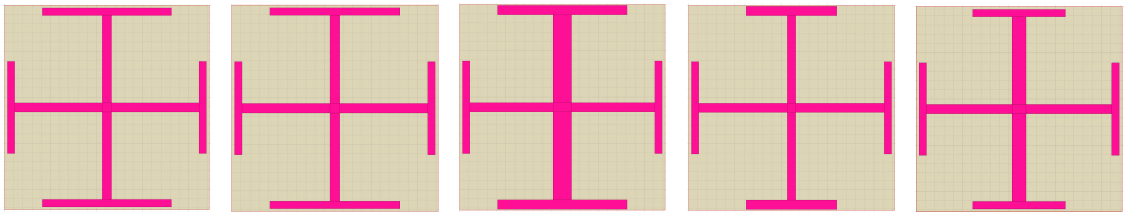

(a) 36^o (b) 108^o (c) -180^o (d) -108^o (e) -36^o

Figure 4.9: Top and bottom layer of unit cell for each phase

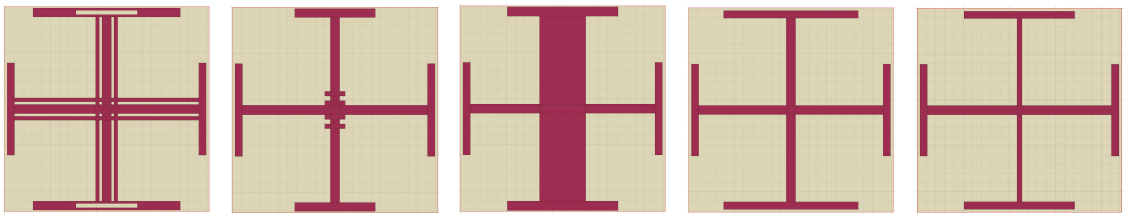

(a) 36^o (b) 108^o (c) -180^o (d) -108^o (e) -36^o

Figure 4.10: Middle layer of unit cell for each phase

Each unit cell is simulated with periodic boundaries. The discussed parameters effect the x-polarization. The magnitude and phase of the transmission coefficient for both the polarization of each unit cell are listed in Table 4.2 where mode 1 is y polarization and mode 2 is x polarization.

The magnitudes of the second mode are substantial, whereas the magnitude of mode 1 are negligible. There is some consistency in the phase for mode 1, but that does not effect mode 2 since the magnitude corresponding to those phases are so small. The full metasurface will be created using these five unit cell measurements. The parameters discussed will be used to define the admittance and phase profile for the

Table 4.2: Phase and Magnitude for Mode 1 and 2 For Each Unit Cell

Goal ϕ	**Mode 1** ϕ	**Mode 2** ϕ	**Mode 1** $\lvert S_{21}\rvert$	**Mode 2** $\lvert S_{21}\rvert$
36^o	-92.6^o	40.8^o	0.0858	0.9170
108^o	76.1^o	108.2^o	0.0947	0.7484
-180^o	-94.3^o	-178.4^o	0.0485	0.8878
-108^o	75.7^o	-107.1^o	0.1001	0.8381
-36^o	75.9^o	-35.3^o	0.1001	0.8729

x-polarization. The orthogonal geometries will be adjusted to create the admittance and phase profile for the y-polarization.

CHAPTER 5: CONCLUSION

This thesis presented two different applications of modulated metasurfaces for RF application fabricable with additive manufacturing. The first metasurface presented was a sinusoidally modulated leaky wave antenna with designs for a fully metallic and fully dielectric antenna. The metallic and dielectric antenna had comparable results showing that the same behavior can be achieved with a material ranging from a very low permitivity to infinite permitivity. The antenna was also shown to operate with different pointing angles. The metallic antenna performed perfectly with a pointing angle at the designed value with gain. The electric field attenuated with leaky wave behavior and dissipated by the edge of the antenna. The dielectric antenna designed for non-broadside propagation performed as predicted. The antenna was rotated 180^o and was able to operate efficiently with a backward radiation. The initial dielectric antennas were simulated using the permitivity of a common additive manufacturing filament, but the metallic was simulated using PEC. The results of the PEC antenna at broadside were compared to the conductive filament metallic broadside antenna and the results were practically identical proving the feasibility of fabricating both the metallic and dielectric antenna with a commercial 3D printer. This antenna design can be utilized for wireless technology and space applications such as satellites and space and Earth observation. In addition, the dielectric antenna is a low-cost, light weight, easily fabricable alternative to a traditionally heavy and higher priced antenna.

The second metasurface presented is a three-layer polarization splitter. The unit cells are designed to be able to compensate any beam angle providing a full range of phase. Each cell was demonstrated to produce a specific phase. The beam steering

angle of the metasurface is dependent on whether the screen is excited with a TE or TM wave. The results proved that a dual polarization metasurface is feasible with independent impedance profiles based on excitation. With most metasurfaces currently available being singularly polarized, this metasurface introduces the second polarization allowing for more control and customization of design.

REFERENCES

[1] "periodic table,"

[2] R. Schittny, M. Kadic, S. Guenneau, and M. Wegener, "Experiments on transformation thermodynamics: Molding the flow of heat," *Physical Review Letters*, vol. 110, May 2013.

[3] K. Muamer, T. Buckmann, R. Schittny, and M. Wegener, "Metamaterials beyond electromagnetism," *Reports on progress in physics. Physical Society (Great Britain)*, vol. 76, p. 126501, 11 2013.

[4] Z. Liang and J. Li, "Extreme acoustic metamaterial by coiling up space," *Physical review letters*, vol. 108, p. 114301, 03 2012.

[5] T. Buckmann, N. Stenger, M. Kadic, J. Kaschke, A. Frolich, T. Kennerknecht, C. Eberl, M. Thiel, and M. Wegener, "Tailored 3d mechanical metamaterials made by dip-in direct-laser-writing optical lithography," *Advanced Materials*, vol. 24, no. 20, pp. 2710–2714, 2012.

[6] D. Smith, W. Padilla, D. Vier, S. Nemat-Nasser, and S. Schultz, "Composite medium with simultaneously negative permeability and permittivity," *Physical review letters*, vol. 84, pp. 4184–7, 05 2000.

[7] R. A. Shelby, D. R. Smith, and S. Schultz, "Experimental verification of a negative index of refraction," *Science*, vol. 292, no. 5514, pp. 77–79, 2001.

[8] V. Tiukuvaara, T. J. Smy, and S. Gupta, "Metasurface modeling of periodic diffraction gratings based on generalized sheet transition conditions (gstcs)," in *2020 14th European Conference on Antennas and Propagation (EuCAP)*, pp. 1–4, 2020.

[9] C. Pfeiffer and A. Grbic, "Bianisotropic metasurfaces for optimal polarization control: Analysis and synthesis," *Phys. Rev. Applied*, vol. 2, p. 044011, Oct 2014.

[10] John L. Volakis, Arthur A Oliner, and David R. Jackson, *Antenna Engineering Handbook*. McGraw-Hill Education, 2007.

[11] G. Minatti, M. Faenzi, E. Martini, F. Caminita, P. De Vita, D. GonzÃ¡lez-Ovejero, M. Sabbadini, and S. Maci, "Modulated metasurface antennas for space: Synthesis, analysis and realizations," *IEEE Transactions on Antennas and Propagation*, vol. 63, no. 4, pp. 1288–1300, 2015.

[12] G. Minatti, S. Maci, P. De Vita, A. Freni, and M. Sabbadini, "A circularly-polarized isoflux antenna based on anisotropic metasurface," *IEEE Transactions on Antennas and Propagation*, vol. 60, no. 11, pp. 4998–5009, 2012.

[13] Manabendra N. Bera, Arnau Riera, Maciej Lewenstein Andreas Winter, "Generalized laws of thermodynamics in the presence of correlations," *nature communications*, 2017.

[14] S. Narayana and Y. Sato, "Heat flux manipulation with engineered thermal materials," *Physical Review Letters*, vol. 108, 05 2012.

[15] S. Guenneau and T. Puvirajesinghe, "Fick's second law transformed: One path to cloaking in mass diffusion," *Journal of the Royal Society, Interface / the Royal Society*, vol. 10, p. 20130106, 03 2013.

[16] J. Li and C. Chan, "Double-negative acoustic metamaterial," *Physical review. E, Statistical, nonlinear, and soft matter physics*, vol. 70, p. 055602, 12 2004.

[17] Y. Xie, B.-I. Popa, L. Zigoneanu, and S. A. Cummer, "Measurement of a broadband negative index with space-coiling acoustic metamaterials," *Phys. Rev. Lett.*, vol. 110, p. 175501, Apr 2013.

[18] N. Jones, "Three-dimensional printers are opening up new worlds to research," *Nature*, vol. 487, pp. 22–23, July 2012.

[19] T. Frenzel, J. Brehm, T. BÃŒckmann, R. Schittny, K. Muamer, and M. Wegener, "Three-dimensional labyrinthine acoustic metamaterials," *Applied Physics Letters*, vol. 103, p. 061907, 08 2013.

[20] S. Zhang, W. Fan, N. C. Panoiu, K. J. Malloy, R. M. Osgood, and S. R. J. Brueck, "Experimental demonstration of near-infrared negative-index metamaterials," *Phys. Rev. Lett.*, vol. 95, p. 137404, Sep 2005.

[21] N. Fang, D. Xi, J. Xu, M. Ambati, W. Srituravanich, C. Sun, and X. Zhang, "Ultrasonic metamaterials with negative modulus," *Nature materials*, vol. 5, pp. 452–6, 07 2006.

[22] S. Zhang, C. Xia, and N. Fang, "Broadband acoustic cloak for ultrasound waves," *Phys. Rev. Lett.*, vol. 106, p. 024301, Jan 2011.

[23] L. Sanchis, V. M. García-Chocano, R. Llopis-Pontiveros, A. Climente, J. Martínez-Pastor, F. Cervera, and J. Sánchez-Dehesa, "Three-dimensional axisymmetric cloak based on the cancellation of acoustic scattering from a sphere," *Phys. Rev. Lett.*, vol. 110, p. 124301, Mar 2013.

[24] T. Schaedler, A. Jacobsen, A. Torrents, A. Sorensen, J. Lian, J. Greer, L. Valdevit, and W. Carter, "Ultralight metallic microlattices," *Science (New York, N.Y.)*, vol. 334, pp. 962–5, 11 2011.

[25] R. Shahar, P. Zaslansky, M. Barak, A. Friesem, J. Currey, and S. Weiner, "Anisotropic poisson's ratio and compression modulus of cortical bone determined by speckle interferometry," *Journal of Biomechanics*, vol. 40, no. 2, pp. 252 – 264, 2007.

[26] G. W. Milton, "Complete characterization of the macroscopic deformations of periodic unimode metamaterials of rigid bars and pivots," *Journal of the Mechanics and Physics of Solids*, vol. 61, no. 7, pp. 1543 – 1560, 2013.

[27] T. BÃŒeckmann, R. Schittny, M. Thiel, K. Muamer, G. Milton, and M. Wegener, "On three-dimensional dilational elastic metamaterials," *New Journal of Physics*, vol. 16, p. 033032, 03 2014.

[28] N. Stenger, M. Wilhelm, and M. Wegener, "Experiments on elastic cloaking in thin plates," *Phys. Rev. Lett.*, vol. 108, p. 014301, Jan 2012.

[29] R. Schmied, J. Halimeh, and M. Wegener, "Conformal carpet and grating cloaks," *Optics express*, vol. 18, pp. 24361–7, 11 2010.

[30] G. Milton and A. Cherkaev, "Which elasticity tensors are realizable?," *Journal of Engineering Materials and Technology-transactions of The Asme - J ENG MATER TECHNOL*, vol. 117, 10 1995.

[31] P. G. Martinsson and A. B. Movchan, "Vibrations of lattice structures and phononic band gaps," *Quarterly Journal of Mechanics and Applied Mathematics*, vol. 56, no. 1, pp. 45–64, 2003.

[32] C. N. Layman, C. J. Naify, T. P. Martin, D. C. Calvo, and G. J. Orris, "Highly anisotropic elements for acoustic pentamode applications," *Phys. Rev. Lett.*, vol. 111, p. 024302, Jul 2013.

[33] A. N. a. Norris, "Acoustic metafluids," *The Journal of the Acoustical Society of America*, vol. 125, no. 2, pp. 839–849, 2009.

[34] V. G. Veselago, "The electrodynamics of substances with simultaneously negative values of ϵ and μ," *Phys. Usp.*, vol. 10, no. 4, pp. 509–514, 1968.

[35] J. B. Pendry, A. J. Holden, D. J. Robbins, and W. J. Stewart, "Magnetism from conductors and enhanced nonlinear phenomena," *IEEE Transactions on Microwave Theory and Techniques*, vol. 47, no. 11, pp. 2075–2084, 1999.

[36] J. B. Pendry, D. Schurig, and D. R. Smith, "Controlling electromagnetic fields," *Science*, vol. 312, no. 5781, pp. 1780–1782, 2006.

[37] D. R. Smith, J. B. Pendry, and M. C. K. Wiltshire, "Metamaterials and negative refractive index," *Science*, vol. 305, no. 5685, pp. 788–792, 2004.

[38] S. A. Cummer, B.-I. Popa, D. Schurig, D. R. Smith, and J. Pendry, "Full-wave simulations of electromagnetic cloaking structures," *Phys. Rev. E*, vol. 74, p. 036621, Sep 2006.

[39] M. McCall, A. Favaro, P. Kinsler, and A. Boardman, "A spacetime cloak, or a history editor," *J. Opt. JOURNAL OF OPTICS J. Opt*, vol. 13, pp. 24003–9, 02 2011.

[40] C. M. Soukoulis and M. Wegener, "Past achievements and future challenges in the development of three-dimensional photonic metamaterials," *Nature Photonics*, vol. 5, pp. 523–530, Sept. 2011.

[41] H.-T. Chen, A. Taylor, and N. yu, "A review of metasurfaces: Physics and applications," *Reports on Progress in Physics*, vol. 79, 05 2016.

[42] A. Oliner and A. Hessel, "Guided waves on sinusoidally-modulated reactance surfaces," *IRE Transactions on Antennas and Propagation*, vol. 7, no. 5, pp. 201–208, 1959.

[43] D. GonzÃ¡lez-Ovejero, C. Jung-Kubiak, M. Alonso-delPino, T. Reck, and G. Chattopadhyay, "Design, fabrication and testing of a modulated metasurface antenna at 300 ghz," in *2017 11th European Conference on Antennas and Propagation (EUCAP)*, pp. 3416–3418, 2017.

[44] B. H. Fong, J. S. Colburn, J. J. Ottusch, J. L. Visher, and D. F. Sievenpiper, "Scalar and tensor holographic artificial impedance surfaces," *IEEE Transactions on Antennas and Propagation*, vol. 58, no. 10, pp. 3212–3221, 2010.

[45] S. Ramalingam, C. A. Balanis, C. R. Birtcher, and S. Pandi, "Analysis and design of checkerboard leaky-wave antennas with low radar cross section," *IEEE Open Journal of Antennas and Propagation*, vol. 1, pp. 26–40, 2020.

[46] D. GonzÃ¡lez-Ovejero, N. Chahat, R. Sauleau, G. Chattopadhyay, S. Maci, and M. Ettorre, "Additive manufactured metal-only modulated metasurface antennas," *IEEE Transactions on Antennas and Propagation*, vol. 66, no. 11, pp. 6106–6114, 2018.

[47] G. Floquet, "Sur les équations différentielles linéaires à coefficients périodiques," *Annales scientifiques de l'École Normale Supérieure*, vol. 2e série, 12, pp. 47–88, 1883.

[48] F. Bloch, "Über die Quantenmechanik der Elektronen in Kristallgittern," *Zeitschrift fur Physik*, vol. 52, pp. 555–600, July 1929.

[49] A. Mohsen, "On the impedance boundary condition," *Applied Mathematical Modelling*, vol. 6, no. 5, pp. 405 – 407, 1982.

[50] T. B. A. Senior, "Impedance boundary conditions for imperfectly conducting surfaces," *Springer Nature*, Jan. 1960.

[51] G. Minatti, F. Caminita, M. Casaletti, and S. Maci, "Spiral leaky-wave antennas based on modulated surface impedance," *IEEE Transactions on Antennas and Propagation*, vol. 59, no. 12, pp. 4436–4444, 2011.

[52] C. L. Holloway, E. F. Kuester, J. A. Gordon, J. O'Hara, J. Booth, and D. R. Smith, "An overview of the theory and applications of metasurfaces: The two-dimensional equivalents of metamaterials," *IEEE Antennas and Propagation Magazine*, vol. 54, no. 2, pp. 10–35, 2012.

[53] C. Pfeiffer and A. Grbic, "Millimeter-wave transmitarrays for wavefront and polarization control," *IEEE Transactions on Microwave Theory and Techniques*, vol. 61, no. 12, pp. 4407–4417, 2013.

[54] F. Monticone, N. Mohammadi Estakhri, and A. Alu, "Full control of nanoscale optical transmission with a composite metascreen," *Physical Review Letters*, vol. 110, pp. 203903–, 05 2013.

[55] D. M. Pozar, *Microwave Engineering*. Wiley, 2017.